RESEARCH ARTICLE

Thermal Nature of Mantle Upwellings Below the Ibero-Western Maghreb Region Inferred From Teleseismic Tomography

Chiara Civiero[1,2] [ID], Susana Custódio[1], Nicholas Rawlinson[3] [ID], Vincent Strak[4], Graça Silveira[1,5] [ID], Pierre Arroucau[6], and Carlos Corela[1]

[1]Instituto Dom Luiz, Faculdade de Ciências, Universidade de Lisboa, Lisbon, Portugal, [2]Dublin Institute for Advanced Studies, Dublin, Ireland, [3]Department of Earth Sciences - Bullard Laboratories, University of Cambridge, Cambridge, UK, [4]Department of Earth Sciences, Vrije Universiteit Amsterdam, Amsterdam, Netherlands, [5]Instituto Superior de Engenharia de Lisboa, Lisbon, Portugal, [6]EDF/DIPNN/DI/TEGG/SGG, Groupe Aléa Sismique, Aix-en-Provence, France

Abstract Independent models of *P* wave and *S* wave velocity anomalies in the mantle derived from seismic tomography help to distinguish thermal signatures from those of partial melt, volatiles, and compositional variations. Here we use seismic data from SW Europe and NW Africa, spanning the region between the Pyrenees and the Canaries, in order to obtain a new *S-SKS* relative arrival-time tomographic model of the upper mantle below Iberia, Western Morocco, and the Canaries. Similar to previous *P* wave tomographic results, the *S* wave model provides evidence for (1) subvertical upper-mantle low-velocity structures below the Canaries, Atlas Ranges, and Gibraltar Arc, which are interpreted as mantle upwellings fed by a common lower-mantle source below the Canaries; and (2) two low-velocity anomalies below the eastern Rif and Betics that we interpret as the result of the interaction between quasi-toroidal mantle flow induced by the Gibraltar slab and the mantle upwelling behind it. The analysis of teleseismic *P* wave and *S* wave arrival-time residuals and the conversion of the low-velocity anomalies to temperature variations suggest that the upwellings in the upper mantle below the Canaries, Atlas Ranges, and Gibraltar Arc system may be solely thermal in nature, with temperature excesses in the range ~100–350 °C. Our results also indicate that local partial melting can be present at lithospheric depths, especially below the Atlas Ranges. The locations of thermal mantle upwellings are in good agreement with those of thinned lithosphere, moderate to high heat-flow measurements, and recent magmatic activity at the surface.

1. Introduction

Traveltime tomography exploits information contained within seismic data sets in order to constrain seismic velocity anomalies associated with variations in Earth's internal structure. Seismic velocity heterogeneities can result from variations in temperature, chemical composition, partial melt and volatile content, anisotropy and grain size (Cammarano et al., 2005; Faul & Jackson, 2002; Karato & Jung, 1998; Schmandt & Humphreys, 2010b). An ongoing challenge in imaging the Earth's internal structure is to infer the degree to which each of these mechanisms contributes to a velocity anomaly. Aided by continuous improvements in the quantity of seismic data and developments in inversion techniques, numerous studies have attempted to infer the nature of seismic velocity anomalies. The independent inversion of *P* wave and *S* wave velocity anomalies can be exploited to gain insight into the physical origin of anomalies. Importantly, the ratio of relative changes in shear to compressional wave velocities, defined as $R_{S,P} = \mathrm{d}\ln V_S/\mathrm{d}\ln V_P = (\mathrm{d}V_S/V_S)/(\mathrm{d}V_P/V_P)$ has been used as an indicator of the physical causes of the observed velocity variations (Cammarano et al., 2003; Masters et al., 2000; Resovsky & Trampert, 2003; Robertson & Woodhouse, 1996; Saltzer et al., 2001; Simmons et al., 2009). Geophysical and mineral-physics studies suggest that mantle temperature variations produce $R_{S,P}$ of magnitudes in the range 1.1–2.2 (Cammarano et al., 2003; Goes et al., 2000; Koper et al., 1999). The effect of composition on V_P and V_S is small compared to that of temperature (for most plausible compositions) because of the very strong temperature sensitivity and therefore distinguishing between the two remains complicated (Goes et al., 2000). The presence of melt is known to have the strongest effect on $V_{P,S}$, causing an increase of $R_{S,P}$ up to 4.0, particularly for aligned film-like pores and melt fractions above 1% (Hammond & Humphreys, 2000; Takei, 2002).

AGU
100
ADVANCING EARTH
AND SPACE SCIENCE

Journal of Geophysical Research: Solid Earth

10.1029/2018JB016531

A number of teleseismic studies have measured variations in V_P/V_S by jointly inverting P and S arrival time data sets (e.g., Hammond & Humphreys, 2000; Schmandt & Humphreys, 2010a). A recent work by Papaleo et al. (2018) estimated V_P/V_S from teleseismic data that constrain relative rather than absolute velocities; for this approach to be successful, accurate estimates of the background P wave and S wave velocity structure are required. However, both P wave and S wave velocity models are often not available for the same region and when they are, limitations arising from the resolving power of the tomography contaminate $R_{S,P}$ estimates (e.g., Deschamps & Trampert, 2003). When one or both P wave and S wave velocity models lack good resolution, it is preferable to compare directly P wave and S wave relative arrival-time residuals, for common earthquake-station pairs (e.g., Bastow et al., 2005). This approach avoids difficulties related to the varying amplitude recovery of velocity anomalies (e.g., due to differing numbers of traveltime observations, different levels of noise, and different regularization parameters) and other issues associated with the underdetermined nature of the tomographic inverse problem. Moreover, the ratio of the arrival-time residuals ($a_{S,P}$) is proportional to the ratio of absolute dV_S and dV_P along the chosen station-event pairs; therefore, the least squares fit of $a_{S,P}$ equals $(V_P/V_S)R_{S,P}$ (Civiero et al., 2016). As this estimate is averaged along the whole path, from source to receiver, the spatial distribution of the anomaly may not be well known. However, if we measure it for several source-station pairs, this limitation can be mitigated.

The computation of $R_{S,P}$ from the ratio of arrival-time residuals was first proposed by Hales and Doyle (1967) who investigated variations in S wave and P wave residuals to infer the presence of melting beneath the western United States. More recently, Rocha et al. (2011) focused on residuals to infer distinct temperature and compositional influences in Brazil. Residual analysis performed for Ethiopia found a slope consistent with purely thermal variations, although in the shallow mantle partial melt is not excluded (Bastow et al., 2005; Civiero et al., 2016).

It has been demonstrated that in the upper mantle seismic velocities are primarily sensitive to temperature and less so to composition (Afonso et al., 2010; Cammarano et al., 2003; Goes et al., 2000; Sobolev et al., 1997). Down to depths of 200 km in the mantle, temperature variations induce strong relative dV_S anomalies, whereas variations in composition generate weaker anomalies. For example, for a 100 °C increase in temperature, a decrease of 0.7–4.5% in V_S is predicted, mostly due to the large effect of anelasticity at high temperature (Goes et al., 2000). The effects of realistic compositional variations instead produce velocity anomalies <1% and are therefore more difficult to retrieve (Goes et al., 2000). As such, while it may be reasonable to interpret dV_S anomalies largely in terms of temperature distribution, it is challenging to make meaningful inferences about compositional variations (Forte & Perry, 2000). The amplitudes of tomographic velocity anomalies can thus be scaled to temperature anomalies (e.g., Cammarano et al., 2003; Goes et al., 2000; Sobolev et al., 1996; Yan et al., 1989) under the assumption that compositional variations are second order. Using this reasoning, independent P wave and S wave tomographic models have been used to infer the thermal structure of the upper mantle below North America (Goes & van der Lee, 2002), Europe (Goes et al., 2000), and Australia (Goes et al., 2005). A similar approach was followed by Currie and Hyndman (2006) for circum-Pacific backarcs and by Civiero et al. (2015, 2016) for Ethiopia, using different mantle composition assumptions.

In this study we address the seismic and thermal structure of the upper mantle below the Ibero-western Maghreb. This region, located between the western Mediterranean Sea and central-eastern Atlantic Ocean, has a complex tectonic history resulting from the convergence between the African and Eurasian plates (Lonergan & White, 1997). The western margin of Iberia, covered by Paleozoic outcrops, forms the Iberian massif that has been geologically stable for the last 300 Ma (Gibbons & Moreno, 2002). The Valencia trough, a Neogene SW-NE oriented extensional basin, delimits the region offshore to the east-northeast (Fontboté et al., 1990). The Iberian-European plate boundary is represented by the Pyrenees, an orogen resulting from the collision of the two plates during the Cretaceous and Miocene (Choukroune, 1989). Southward, the Gibraltar Arc System includes different structures such as the Alboran basin and the Betic-Rif orogen (Gutscher et al., 2002). South of the Rif, the intracontinental Atlas Mountains consist of Paleozoic, Mesozoic, and Cenozoic rocks with summits that exceed 4,000-m elevation (e.g., Zeyen et al., 2005, Figure 1a).

Existing S wave models for the region have been obtained by finite-frequency Rayleigh wave tomography (e.g., Palomeras et al., 2014; Peter et al., 2008; Schivardi & Morelli, 2009). However, the depth extent of these models is more limited than that achieved by body wave traveltime tomography. As a result, a
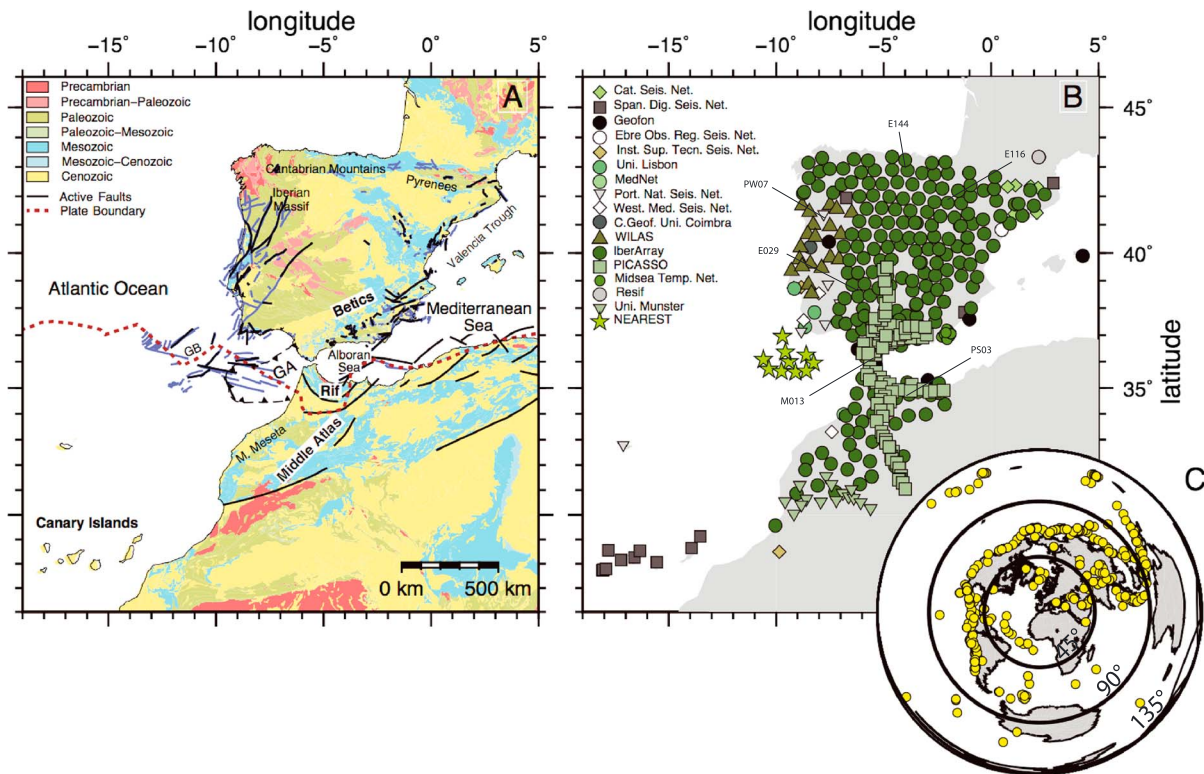
Figure 1. (a) Geological units of the Ibero-western Maghreb region (from https://pubs.usgs.gov/dds/dds-060/), Eurasia-Africa plate boundary (brown, Bird, 2003), potentially active faults from the SHARE database (black, Basili et al., 2013; Vilanova et al., 2014) and high-resolution fault traces (including debated faults; blue, Cabral, 2012; García-Mayordomo et al., 2012; Zitellini et al., 2009). The geographic features cited in the text are indicated in black. GA = Gibraltar arc; GB = Gorringe Bank. (b) Location of the seismic stations used in this study. Colors and symbols mark the different seismic networks. The six labeled stations are those for which residuals are shown in Figure S1. (c) Distribution of the teleseismic events used (yellow dots).

comprehensive view of the upper mantle, as given by similarly resolved *P* wave and *S* wave velocity models, is not available. In this study, we present the first teleseismic traveltime tomography model that images *S* wave velocities at high resolution down to the base of the mantle transition zone (MTZ). We further present a comparison with the *P* wave velocity structure already imaged in a companion study (Civiero et al., 2018), which we will refer to as IBEM-P18. Finally, we investigate the nature of the low-velocity anomalies by analyzing *P* wave and *S* wave arrival-time residuals and by converting the velocity anomalies to temperature estimates using a mineral-physics approach.

2. Data and Method

2.1. Data Sets

We used relative arrival-time residuals of teleseismic *S* and *SKS* phases observed at 410 broadband seismic stations deployed in the Ibero-western Maghreb region to invert for 3D *S* wave velocity perturbations in the mantle (Figure 1). The inclusion of *SKS* phases into the *S* wave traveltime tomography provides additional, steeper, crossing paths down to the MTZ. The ensemble of stations used encompassed 203 stations from the IberArray deployment (Díaz et al., 2009), 91 from the PICASSO array (Platt et al., 2008), 20 from the WILAS project (Custódio et al., 2014), and 10 ocean-bottom seismometers (OBSs) deployed by the NEAREST experiment (Carrara and NEAREST Team, 2008). An additional 86 temporary and permanent instruments from another 13 seismic networks were also used. In total, we used data from 17 international seismic experiments and permanent networks that operated over the course of 6 years, from 2007 to 2013. Detailed information about the stations is available in the supporting information Table S1. We selected 380 high-quality teleseismic earthquakes with magnitudes larger than 5.5 and epicentral distances of 30–135° (30–95° for *S* phases and 95–135° for *SKS* phases).

Relative arrival-time residuals were estimated using an adaptive stacking technique developed by Rawlinson and Kennett (2004), which exploits the coherency in the arriving waveforms across the array. We first filtered seismograms by applying a 0.04- to 4-Hz band-pass Butterworth filter. Subsequently, the data were rotated into radial and tangential components and residuals were obtained for direct S phases observed on the tangential component and for SKS phases observed on the radial component. The automatic process was complemented by a visual inspection of the waveforms that ensured the selection of high-quality measurements only. After the rejection of poor-quality data, our data set comprised 15,619 S wave and SKS wave relative arrival-time residuals. The residuals range from approximately −5 to 5 s. Further details on the arrival-time residual estimation, the back-azimuthal variation of the residuals for a selection of stations located in different parts of the Ibero-western Maghreb region and the epicentral distance distributions are shown in supporting information S1.

2.2. Model Parameterization and Inversion Method

We adopt the same grid spacing used for IBEM-P18 by Civiero et al. (2018), with 0.4° node spacing in latitude (from 26°N to 46°N) and longitude (from 19°W to 5°E) and ~35-km spacing in depth, extending from the Moho down to 800-km depth.

Relative arrival-time residuals were inverted using the FMTOMO package (Rawlinson et al., 2006) to recover the mantle seismic structure. FMTOMO applies the Tau-P method (Kennett & Engdahl, 1991) to compute traveltimes from the source to the edge of the 3D model region. It then combines the Fast Marching Method as a forward solver (Rawlinson & Sambridge, 2004a, 2004b), which tracks the evolving wavefront from the edge of the local 3D model to the receivers at the surface, and a subspace inversion technique, which adjusts model parameters to satisfy observations (Kennett et al., 1988).

The 3D starting model for the crust and upper mantle was built by converting the PRISM3D P wave model (Civiero et al., 2018) into an S wave velocity model assuming a V_P/V_S ratio calculated from the 1D ak135 P wave and S wave speed models as a function of depth (Figures S2a and S2b). The initial S wave velocities in the topmost lower mantle (660- to 800-km depth) are those converted from the LLNL global P wave tomographic model of Simmons et al. (2012, Figure S2c). To reduce the effect of the unresolved crustal contributions to the arrival-time residuals, we included in our starting model a realistic a priori 3D crust and Moho model taken from PRISM3D. We also performed two additional inversions using different starting models: the 1D ak135 S wave speed model (Kennett et al., 1995) and the 3D S wave global model (SEMum2) of French et al. (2013). Our final interpretation will be based on the model obtained using PRISM3D as a starting model, although the features we will focus on are clearly present in all three models.

Smoothing (η) and damping (ε) parameters of 5 and 5, respectively, are used and provide the optimum trade-off between data fit and model roughness (Figure S3). However, different choices of η-ε combinations in the neighborhood of our preferred values do not significantly change the pattern of the anomalies. The final S wave model solution reduces differential traveltime variance by 46.71%, from 2.56 to 1.36 s^2.

3. Resolution Tests

We carried out detailed resolution tests in order to assess whether the main features of our S wave tomographic model are actually required by the data. First, we generated a set of synthetic arrival-time residuals by tracing rays through a known test structure. Then, we added Gaussian noise to the synthetic arrival-time residuals (0.4 s standard deviation) of the same order of magnitude as the data noise, which was estimated by the adaptive stacking approach. Finally, we inverted those residuals using the same algorithm and parameterization that is used for the inversion of the actual field data set. The comparison between the synthetic input test model and the recovered output model provides a basis to assess the reliability of the features recovered in the inversion of the field data set.

In this study, we performed two different types of resolution tests. In the first case, we introduced a checkerboard pattern of alternating positive and negative anomalies, with diameter of $\pm$ ~200 km and amplitude of ± 0.50 km/s, separated by a region of zero perturbation (Figure 2). Slices at 250- to 500-km depth through the reconstructed S wave model (Figures 2c and 2d) show a good agreement between the input and recovered models. However, the recovered anomalies do exhibit some vertical smearing along dominant ray paths, especially in the western (Atlantic Ocean) and eastern (east of the Alboran Sea) parts of the model. Bigger
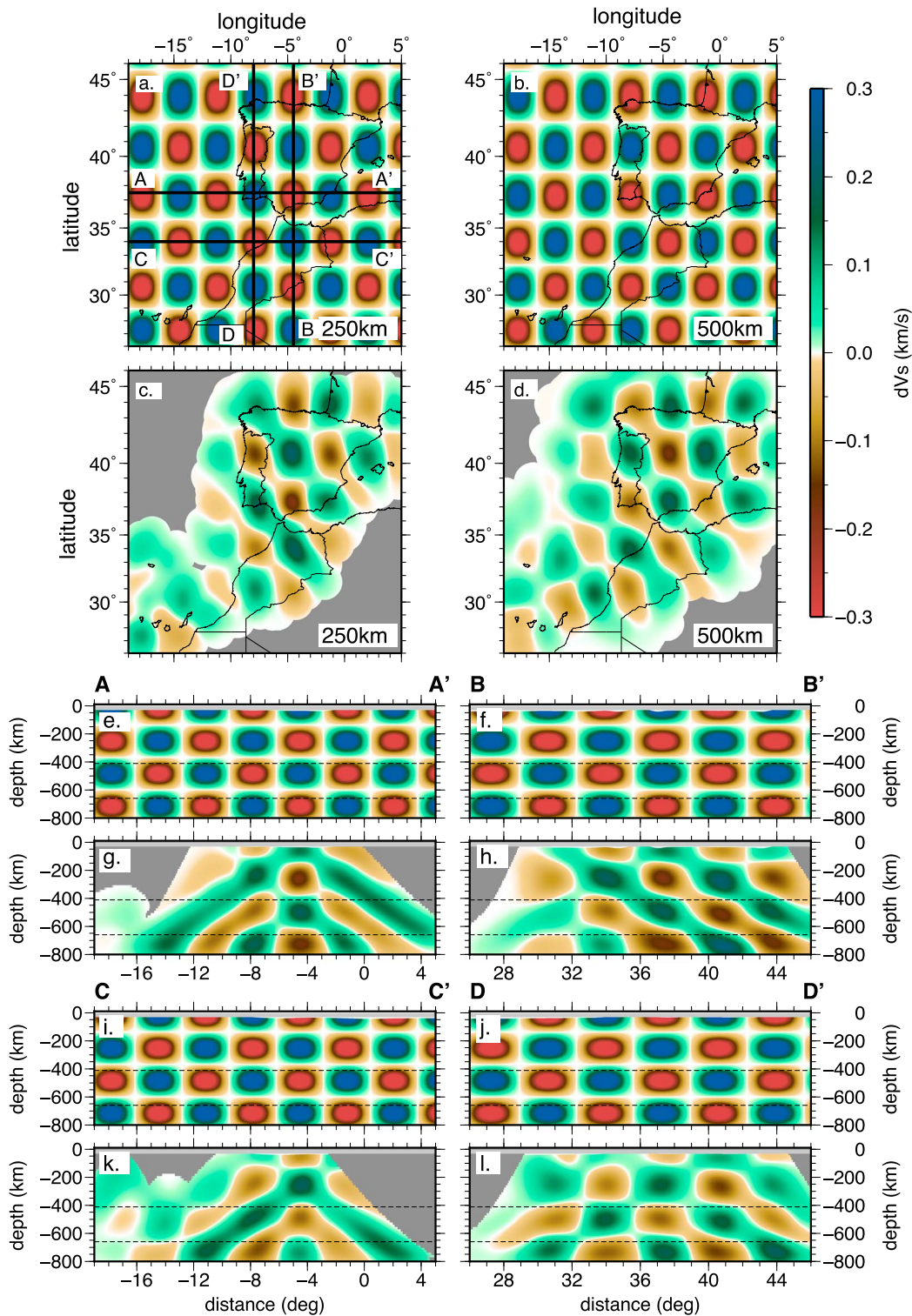
Figure 2. Checkerboard resolution tests for our tomographic study, using alternating positive and negative velocity anomalies of ~200 km width and ±0.5 km/s in amplitude separated by a narrow region of zero perturbation. Velocity perturbations are plotted relative to the 3D starting model. Input model at (a) 250-km and (b) 500-km depth. Output S velocity structure at (c) 250- and (d) 500-km depth. The raypaths and inversion parameters used are the same as in the inversion of actual data. Gaussian noise of 0.4 s is added to the synthetic data set to mimic that of the field data set. Crustal structure is light gray shaded. Regions with no piercing points are shaded darker gray. Black lines show coastlines. Vertical cross sections oriented east-west (e and i) and south-north (f and j), through the input model (orientations of the profiles are shown in depth slice a). (g, h, k, l) Vertical cross sections through the recovered model. These tests suggest a good resolution through the upper mantle for most of the region of interest (the oceanic domain north of the Canaries and the western African craton are excluded from our interpretation).
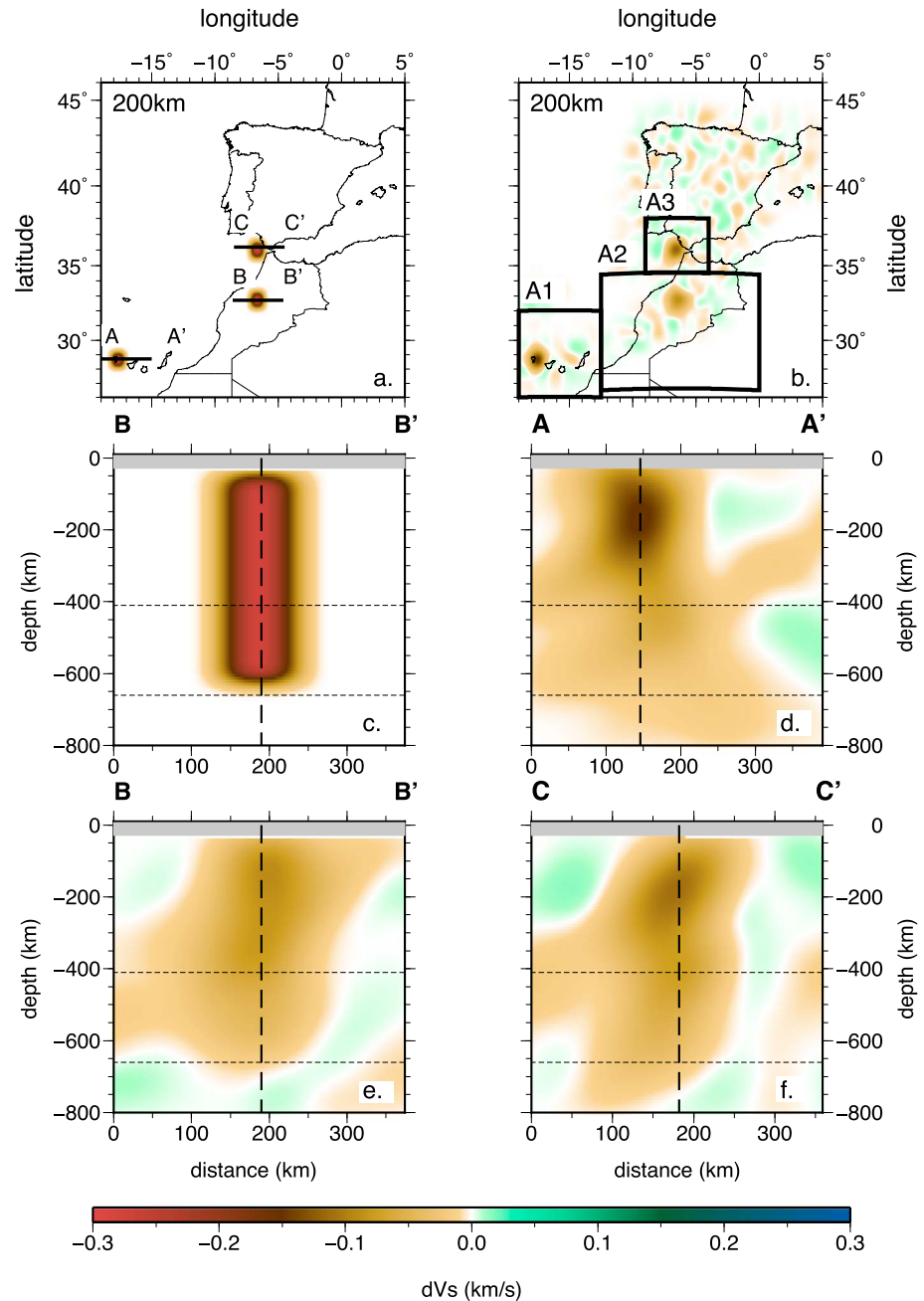
Figure 3. Structural resolution test, using synthetic vertical low-velocity structures below the Canaries (A1), the Atlas Ranges (A2), and the Gibraltar arc (A3; −0.3 km/s amplitude). Velocity perturbations are plotted relative to the 3D starting model. (a) Map view of the input model at 200-km depth. (b) Map view of the recovered model at 200-km depth. Boxes A1–A3 delimit the regions—Canaries, Atlas Ranges, and Gibraltar arc—for which we compute temperature conversions. (c) Input model through vertical cross sections oriented west-east below A2 (the same input structure is located below A1 and A3). The profiles are shown in depth slice a. (d–f) Vertical cross sections through the recovered models. The raypaths and inversion parameters used are the same as for the inversion of actual observations. Gaussian noise with a standard deviation of 0.4 s is added to the synthetic data set to mimic the noise in the observations. Crustal structure is gray shaded. The amplitude recovery of the vertical bodies below A1 (d) and A3 (f) in the depth range 0–200 km is around 35%. The amplitude recovery of the vertical structure below A2 (e) is around 20% down to 450-km depth.

features, with diameters of ~300 km, are still well resolved within the MTZ (Figure S4). The synthetic tests indicate that the S wave data cannot resolve structures as clearly as the P wave data (as demonstrated by a comparison with IBEM-P18, see Figures S5 and S6 in the supporting information), especially below the MTZ. This is a fairly typical outcome, since the S wave residuals tend to be noisier than those of P waves, and the number of arrivals that are picked is lower (Bolton & Masters, 2001).

In the next test we used three vertical structures (amplitude ≈ -0.30 km/s, diameter ~100 km) located approximately below the Canaries (A1), Atlas Ranges (A2), and Gibraltar Arc (A3) as input (Figure 3). The negative synthetic anomalies are positioned where upper-mantle upwellings have been imaged before (Civiero et al., 2018). We will use the resolving power of these simple structures to scale our tomographic model according to the estimated amplitude recovery, before converting to relative temperature anomalies (see section 4.3). In spite of some smearing downward and along a number of oblique ray paths, all structures are well recovered. A1 is the best resolved region, which may result from a good crossing-rays coverage likely due to the stations above A1 being part of a permanent network, with a longer operating period compared to the temporary arrays that span A2 and A3.

4. Results

4.1. S Wave Tomographic Model

Figures 4 and 5 display depth slices and cross sections through our S wave velocity model, ranging from 70-km down to 730-km depth. The dV_S structure overall exhibits a similar pattern of anomalies to dV_P in IBEM-P18, despite the decreased ray coverage.

The model shows a pronounced positive velocity anomaly corresponding to the location of the subducted Gibraltar slab (d$V_S \approx 0.3$ km/s in its core), which dips near vertically in the upper mantle. The shape, dip, and amplitude of the slab are consistent with the P wave results (Civiero et al., 2018). We also observe a prominent high-velocity anomaly below western Iberia and an EW-elongated high-velocity feature beneath the southern Pyrenees, both of which extend through the upper mantle, similar to what was imaged in IBEM-P18. The most notable difference with the IBEM-P18 is the absence of a strong high-velocity anomaly below the Gorringe Bank. This is likely due to the poorer resolution in this offshore area, which may result from the fact that we did not use TOPOMED OBS data in this study because the horizontal components lacked accurate orientations and had a poor signal-to-noise ratio.

In the oceanic domain, a prominent low-velocity anomaly is imaged in the upper mantle below A1 (d$V_S \approx -0.2$ km/s). A2 and A3 also exhibit moderate dV_S ranging from -0.3 in the lithosphere to -0.1 km/s or less within the MTZ, with a similar geometry and vertical continuity to those seen in IBEM-P18. In cross-sections AA′ and CC′ (Figures 5a and 5c) we observe that the low-velocity anomaly in A3 is abruptly truncated to the east when it comes into contact with the high-velocity Gibraltar slab. Importantly, we observe a connection between these three slow anomalies at MTZ depths, as also imaged in IBEM-P18.

Low-velocity anomalies below the Betic-Rif system (d$V_S \approx -0.2$ km/s) are also imaged as previously found in IBEM-P18. They extend through the upper mantle and, together with the slow feature west the Gibraltar slab, they surround the high-velocity body in the Alboran Sea. Similar to what was imaged in IBEM-P18, the slow mantle structures below the Betic-Rif system appear disconnected from the lower mantle, although in some sections the structure seems to extend deeper.

The results of the inversions using the 1D ak135 and the 3D SEMum2 as starting models exhibit the same first-order characteristics as those discussed above (see Figures S7 and S8). The main difference is the magnitude of the features imaged, which are weaker in the first case (ak135 reference model) and much stronger at lithospheric depths in the latter case (3D SEMum2 model, Figures S8a–S8c). The more pronounced anomalies of the latter model are not surprising, given that waveform inversions do not regularize amplitude as strongly as traveltime inversions do. In addition, damping back to a 3D starting model instead of a 1D model means that larger amplitudes will always be favored in the former case (Rawlinson et al., 2010).

4.2. Relative Arrival-Time Residuals

To further explore the nature of the recovered perturbations, $R_{S,P}$ is often calculated directly from the tomographic models (e.g., Cammarano et al., 2003; Karato & Karki, 2001; Saltzer et al., 2001; Takei, 2002).
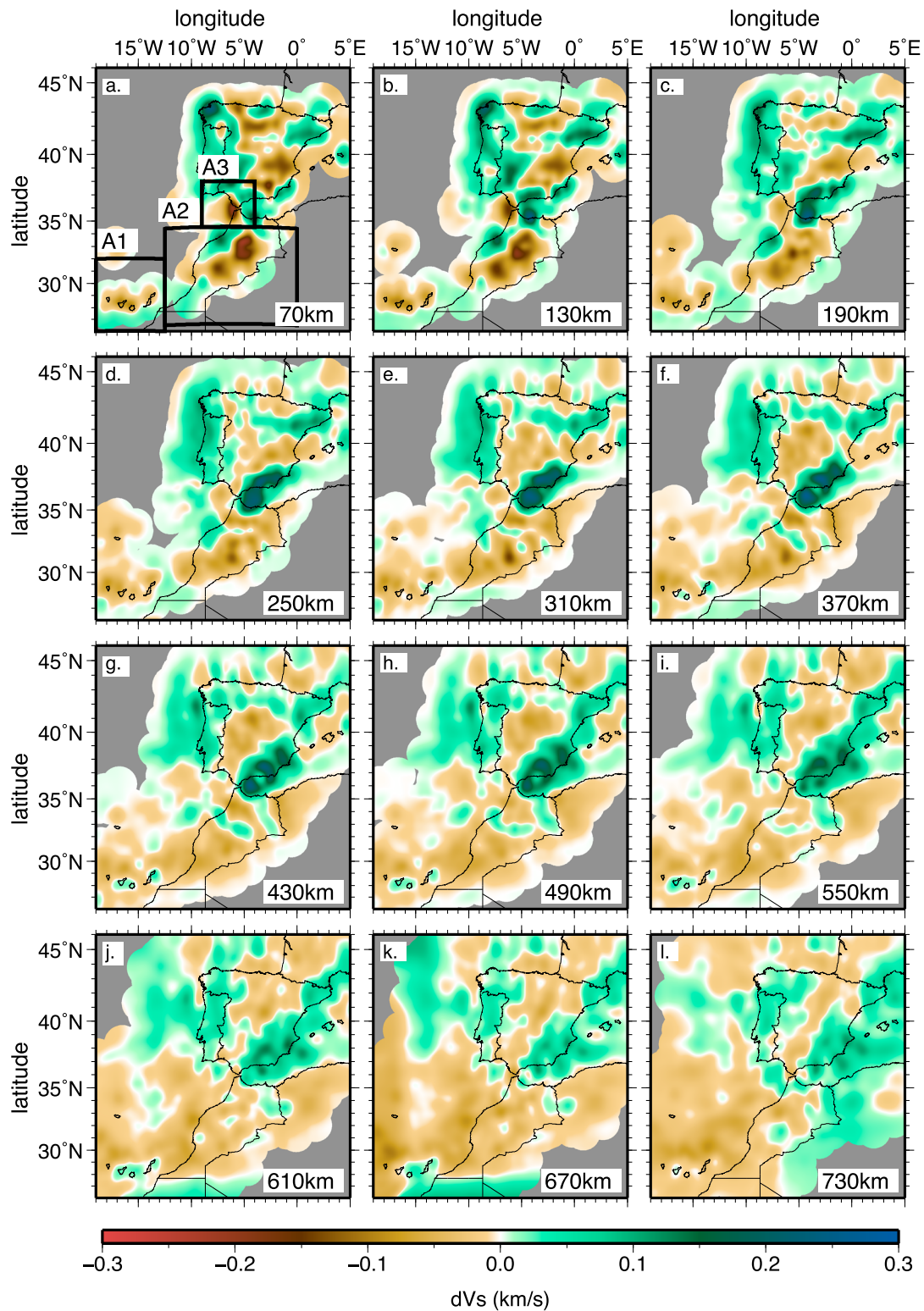
Figure 4. Depth slices through the tomographic *S* wave model at depths between 70 and 730 km. Velocities are plotted relative to a 1D laterally averaged depth-dependent version of the starting model. Regions with no piercing points are shaded gray. Black lines show coastlines. These maps reveal velocity anomalies similar to those imaged in IBEM-P18 (see Figure S5 for comparison). The anomalies discussed in the text are the prominent low-velocity regions below A1–A3 (boxes delimiting the regions are indicated in black in Figure 4a), which extend through the MTZ, and the two low-velocity anomalies below eastern Rif and Betics that surround the high-velocity body below the Alboran Sea.
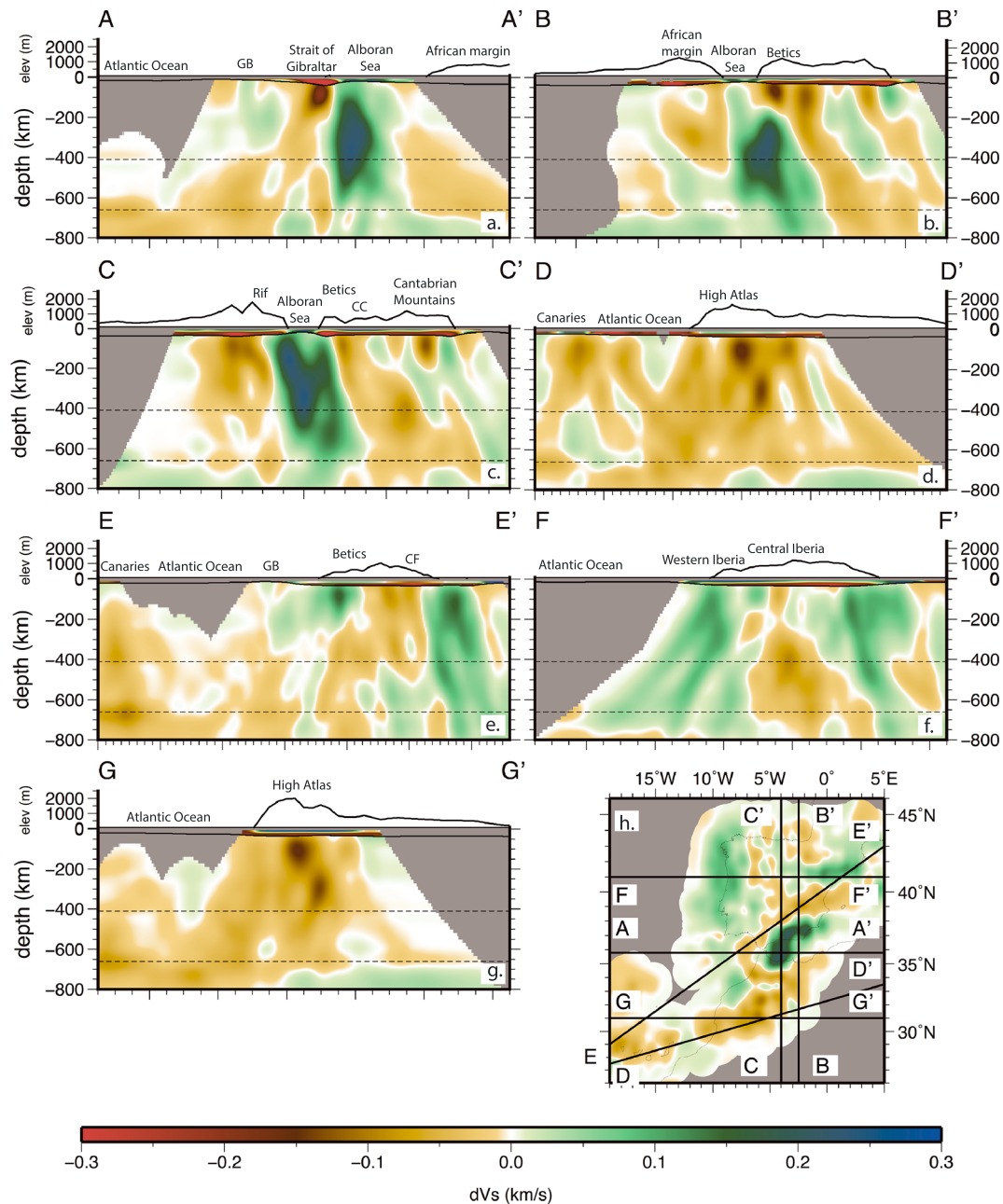
Figure 5. Vertical cross sections through our *S* wave model. The orientation of the profiles is indicated with black lines in the 250-km depth slice. Topography profiles (from Smith & Sandwell, 1997) and geographic names are shown above each cross section. Velocities are plotted relative to a 1D laterally averaged depth-dependent version of the starting model. Regions with no piercing points are shaded gray. The most prominent high-velocity feature is that below the Alboran Sea (profiles a–c). The most relevant low-velocity anomalies, which are discussed in the text, are located below A3 (profile a), below A2 (profiles d and g) and below A1 (profiles e, d and g). These features extend through the MTZ and appear connected at lower-mantle depths.

However, the strong differences in spatial resolution and smearing of our *P* wave and *S* wave models prevent us from using this method. Instead, we compare the *P* wave and *S* wave relative arrival-time residuals for common earthquake-station pairs, thus avoiding difficulties associated with the amplitude recovery of anomalies, potential smearing, spatial resolution dependence on station distribution, and parameterization/regularization. The *P* wave residuals are those of Civiero et al. (2018). Figure 6 shows the *S* wave relative residuals plotted as a function of the *P* wave relative residuals, for stations deployed in the three different areas where we image subvertical low-velocity anomalies extending within the MTZ:
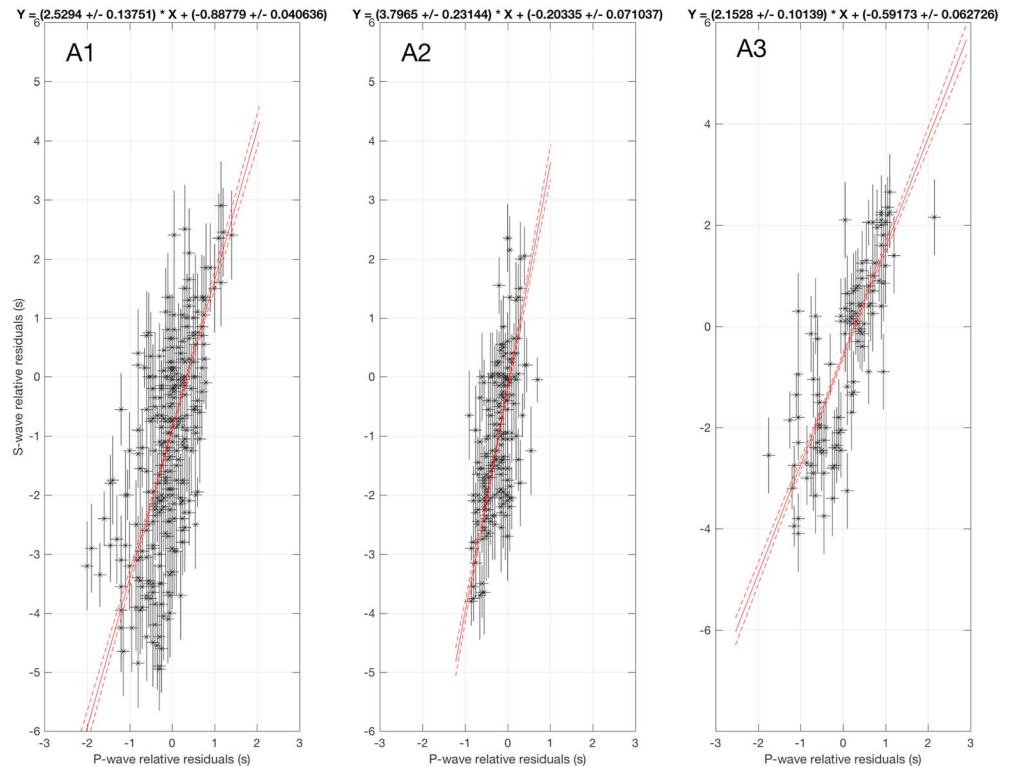
Figure 6. *P* wave (from Civiero et al., 2018) versus *S* wave relative traveltime residuals (with associated errors) for common earthquakes and stations, for stations located in regions A1–A3 (Figure 3). The values of the slopes, $a_{S,P}$, fall within the thermal range for all the selected regions (A1 = ~2.5 ± 0.1; A2 = ~3.8 ± 0.2; A3 = ~2.1 ± 0.1).

A1 (Canaries), A2 (Atlas Ranges), and A3 (Gibraltar Arc). We examine A3 by analyzing *P* wave and *S* wave residuals from stations near the Strait of Gibraltar that record phases that have mainly sampled the Gibraltar Arc. Only the highest-quality data are shown, and outliers identified by visual inspection are removed prior to the analysis (see Table S2). The *P* wave and *S* wave data are calculated independently, but in general show a positive correlation, as expected. In order to fit a straight line through these data, a standard least squares regression model should not be used, because it assumes that there are no errors in *x* (i.e., the *P* wave residuals), which is clearly not the case (see Figure 6). Instead, we apply the LinFitXY tool from MATLAB, which takes into account errors in both *x* (*P* wave residuals) and *y* (*S* wave residuals). This yields a slope $a_{S,P}$, which may be interpreted as a first-order indication of the thermal/chemical origin of the velocity anomalies.

Previous studies using the ratio of *P* wave to *S* wave relative traveltime residuals found that regions with anomalies caused by thermal variations only have $a_{S,P}$ ratios that vary between 1.8 and 2.2 ($R_{S,P}$ = 1.1–1.3, Chung, 1971; Koper et al., 1999). Several other studies found that an $a_{S,P}$ of around 2.9 may be on the high side to invoke only temperature perturbations (e.g., Gao et al., 2004), and values >2.9 likely require the presence of compositional heterogeneities (Rocha et al., 2011). A more recent residual analysis focused on the Afar used a much higher value, with $a_{S,P}$ equal to 3.7, to invoke a thermal origin for the low-velocity anomaly that was imaged (Civiero et al., 2016). However, from our previous discussion of the expected range of $R_{S,P}$ values, $a_{S,P}$ up to ~3.8 can reasonably be interpreted to correspond to an $R_{S,P}$ within the thermal range.

The $a_{S,P}$ in all our regions fall within the range 2.1–3.8 (*A1* = 2.5 ± 0.1; *A2* = 3.8 ± 0.2; *A3* = 2.1 ± 0.1), suggesting that the low-velocity anomalies in the study region are likely due to temperature variations alone. We cannot, however, rule out the possibility that the presence of melt or compositional variations may contribute to the velocity anomalies we detect, especially for A2, which shows an $a_{S,P}$ at the higher end of the thermal range.
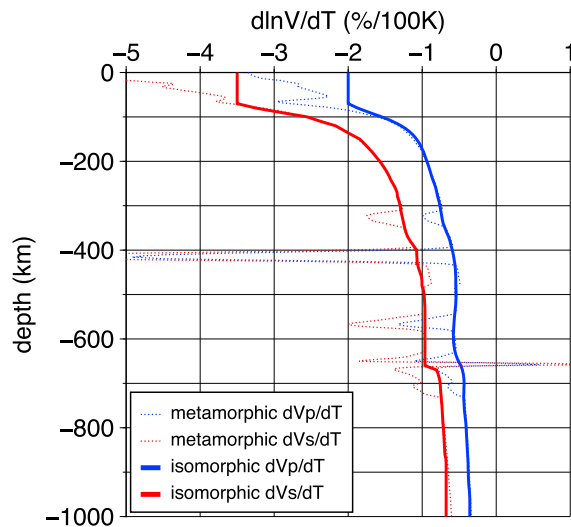
Figure 7. Profiles of the dV_P/dT (blue line) and dV_S/dT (red line) derivatives that we use to convert the recovered velocity to temperature anomalies. The thick profiles correspond to the smoothed isomorphic dV_P/dT and dV_S/dT derivatives, which do not account for effects of phase-boundary topography. The dashed blue and red profiles are, respectively, the metamorphic dV_P/dT and dV_S/dT derivatives, which include the effects of phase transitions. The derivatives were computed along a 1300 °C adiabat for a pyrolite composition using mineral parameters from the database stx08 (Xu et al., 2008), with composite attenuation models Qg (above 400 km, Van Wijk et al., 2008) and Q6 (below 400 km, Goes et al., 2004). For our conversion, we use the isomorphic derivatives because the teleseismic body-wave tomography cannot resolve localized phase-boundary anomalies.

4.3. Velocity-Temperature Conversion

We now convert the seismic-wave anomalies, dV_P and dV_S, of the three low-velocity regions, A1–A3 at 250-km depth, to temperature anomalies following the method described in Civiero et al. (2016). In order to convert the seismic velocities to temperature anomalies, one needs to account for the spatial variability of the seismic resolution, which has implications for the amplitude of the recovered anomalies. A practical way of doing so is to consider the amplitude scaling of the input and output synthetic anomalies. Thus, before proceeding with the velocity to temperature conversion, we scale the P wave and S wave tomographic velocity anomalies according to the amplitude recovery inferred from the center of the three idealized mantle upwelling models (Figures 3 and S9). The amplitude scaling is affected by some uncertainty, because the amplitude recovery depends on the shape of the anomalies and the idealized synthetic structures we use have a simple shape, which likely does not represent the geometries of the real anomalies. Furthermore, the level and distribution of data noise we impose, the choice of model parametrization, and the approximate forward theory we use to compute arrival times will all contribute to uncertainty in the amplitude scaling relationship.

As mentioned in section 1, the low-velocity anomalies in A1–A3 can have different origins, including temperature perturbations, compositional variations, the presence of melt and/or water, grain size, and seismic anisotropy. However, if we assume that the effect of composition on V_P and V_S in the upper mantle is secondary to that of temperature and gains importance only with increasing depth (Cammarano et al., 2003; Goes et al., 2000), then we can interpret the seismic features solely in terms of temperature.

In order to convert to temperature, we use a smooth dV_P/dT and dV_S/dT derivative for a pyrolytic composition along a 1300° adiabat, after the work of Styles et al. (2011, Figure 7). The full (metamorphic) dV/dT that includes the effects of phase transitions is also shown. However, we do not use the latter in our work because such small-scale shifts cannot be resolved with our data set. The sensitivity of seismic velocities to temperature decreases very strongly with depth due to a combination of elastic and anelastic effects (Goes et al., 2004; Styles et al., 2011; Xu et al., 2008). For example, the sensitivity of V_P (V_S) to temperature along a 1300 °C adiabat decreases from ~ −1.55% (−2.5%) per 100 °C at 100 km to ~ − 0.58% (−0.96%) per 100 °C at 600 km. Errors in the isomorphic derivative lead to uncertainties in temperature anomalies of a few tens of degrees (Cammarano et al., 2003; Goes et al., 2000). In Figure 8 we present the resulting thermal structure for P wave and S wave velocity anomalies before and after applying the scaling correction at 250-km depth. As expected, the original temperature anomalies dT_P are higher than dT_S due to the poorer resolution of the S wave model compared to IBEM-P18 (higher noise levels, poorer data coverage, and hence greater regularization). The scaled temperature anomalies dT_P and dT_S are to first order well correlated in all three regions A1–A3. The highest positive thermal contrasts are observed below A2 (dT_S = ~200–350 °C). Beneath A1 and A3, we find weaker temperature anomalies, ranging from ~100 to 300 °C. In the A2 case, the high temperatures together with the high $a_{S,P}$ suggest that nonthermal effects (e.g., partial melt and volatiles) could likely have a contribution to explain the seismic anomaly.

We also plot the temperature estimates by applying the recovery amplitude from the same synthetic structures shown in Figure 3 but with two different maximum velocity amplitude: (i) $dV_{S,P}$ = −0.1 km/s (Figure S10); (ii) $dV_{S,P}$ = −0.6 km/s (Figure S11). These test show that if we change the maximum velocity perturbation we obtain slightly different results in terms of temperature anomaly range. However, the temperature anomalies in A1 and A3 after resolution correction are still in the range ~100–300 °C. The biggest differences appear in the A2 region where in the S wave model the thermal anomaly spans a larger range from ~100–300 (for $dV_{S,P}$ = −0.1 km/s, Figure S10) to ~200–350 °C (Figure 8) and much greater than 400 °C (for $dV_{S,P}$ = −0.6 km/s, Figure S11). This uncertainty likely results from the poorer resolution of the S wave model below A2.
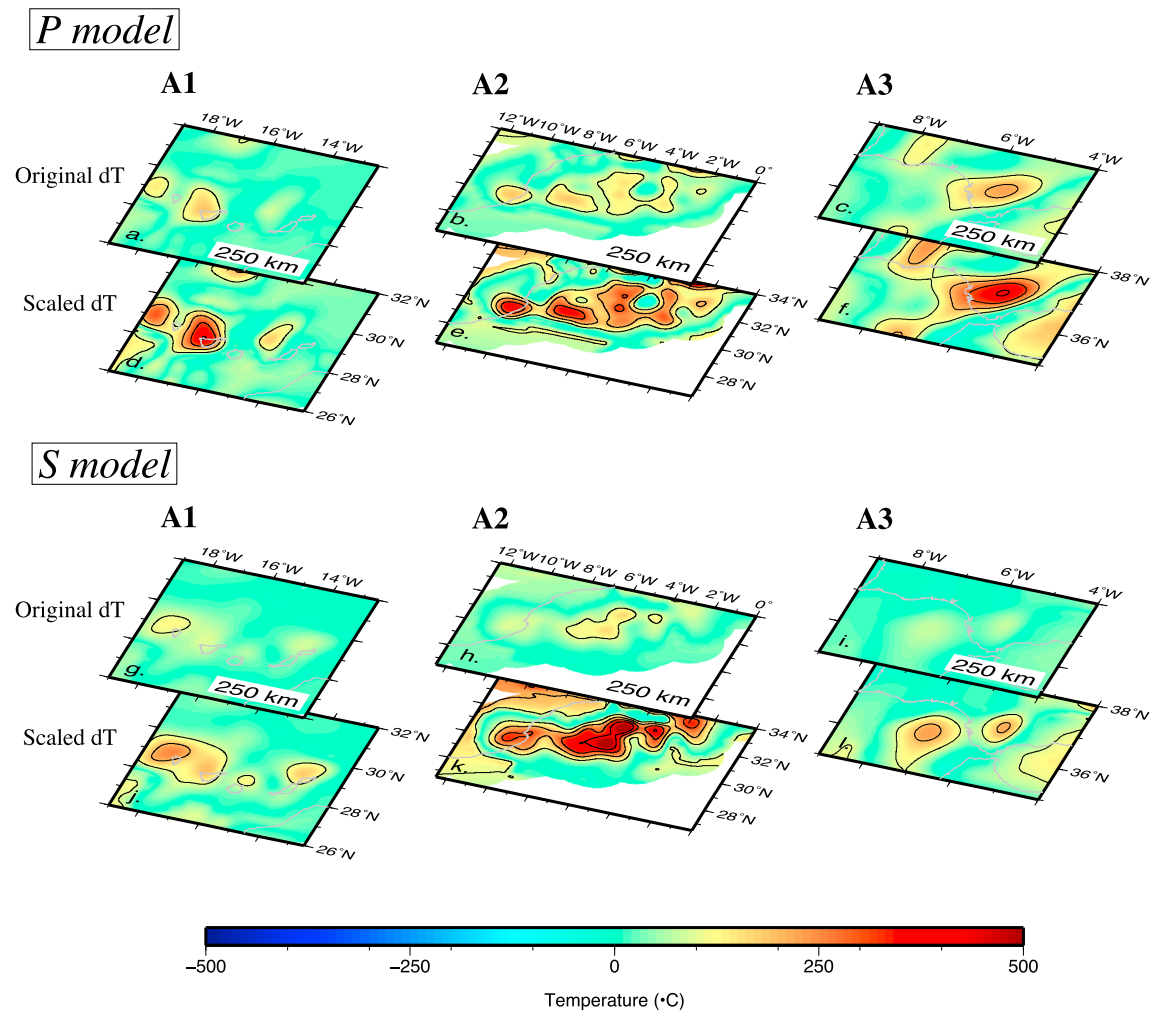
Figure 8. Horizontal slices at 250-km depth showing the thermal anomalies obtained from the conversion of *P* wave and *S* wave velocities using the d*V*/d*T* curves in Figure 7 below the upwellings within A1–A3. (a–c) Original *T* excesses derived from the *P* wave velocities in IBEM-P18 (without accounting for the estimated amplitude recovery). (d–f) Scaled *T* excesses derived from the *P* wave velocities in IBEM-P18 using the estimated amplitude recovery from the resolution test in Figure S9. (g–i) Original *T* excesses derived from the *S* wave velocities (without accounting for the amplitude recovery). (j–l) Scaled *T* excesses derived from the *S* wave velocities using the estimated amplitude recovery from the resolution test in Figure 3. The scaled dT_P and dT_S (d–f and j–l) are to first order well correlated in all three regions A1–A3. Regions with no piercing points are shaded white. Gray lines show coastlines. The spacing between the contours is 100 °C.

5. Discussion

Our computation of independent teleseismic *P* wave and *S* wave velocity models allows us to address key questions concerning the mantle dynamics and physical state of the complex Iberia-NW Africa region. We will limit our interpretation to the upper mantle where our spatial resolution is higher.

5.1. Geodynamical Context

The low-velocity anomalies imaged below the Atlas Ranges and the Betic-Rif system by previous tomographic studies have been attributed to passive mantle upwellings due to edge-driven convection/small-scale convection (e.g., Kaislaniemi & Van Hunen, 2014; Missenard & Cadoux, 2012; Ramdani, 1998) and lithospheric delamination (e.g., Bezada et al., 2014; Levander et al., 2014) or active mantle upwellings connected to the Canary plume (Civiero et al., 2018; Duggen et al., 2009; Miller et al., 2015). In particular, our previous *P* wave model IBEM-P18 allowed us to propose two main mechanisms for the generation of the low-velocity anomalies: (1) The mantle upwellings found below A2 and A3 rise from ~700-km depth and are connected to A1 below the MTZ, with all three being fed by a broad lower-mantle plume (the central Atlantic plume)

imaged in global inversions (e.g., Simmons et al., 2012); and (2) quasi-toroidal mantle flow, induced by the Gibraltar slab, drags the hot mantle material from the subslab upwelling (which is sourced below the MTZ) laterally and upward around either lateral slab edge, to the eastern Rif and Betics. In this latter scenario, the subducted lithospheric slab, which brings cold lithospheric material down into the mantle while rolling back westward, has been associated with the prominent high-velocity body found below the western Alboran Sea. The pronounced low shear velocities that we find in the upper mantle are to first order consistent with the *P* wave low-velocity anomalies found in IBEM-P18 (Civiero et al., 2018). From the base of the MTZ downward, the resolving power of the *S* wave model is inferior to that of IBEM-P18; therefore, any interpretation of the structure in the topmost lower mantle is avoided. However, although we cannot interpret the deeper roots of the anomalies, the structures seem compatible with the presence of multiple upper-mantle upwellings as suggested by IBEM-P18. In line with our previous geodynamical interpretation, we suggest that the *S* wave low-velocity features imaged below A1–A3 are due to rising subvertical upwellings in the upper mantle originating from lower-mantle material located below the Canaries, which accumulates and spreads laterally below the MTZ. As indicated by several numerical and laboratory studies (e.g., Kumagai et al., 2007; Tosi & Yuen, 2011), the 660-km mantle discontinuity resists upward flow of mantle material, which thus ponds just below the discontinuity, heating the overlaying MTZ. In some locations the thermal boundary layer becomes unstable, developing secondary thinner instabilities in the upper mantle. The low-velocity features found beneath the Betic-Rif system may be due to the quasi-toroidal mantle flow created by the rollback of the Gibraltar slab (Funiciello et al., 2006; Piromallo et al., 2006; Strak & Schellart, 2014), which drives the subslab hot mantle upwelling material from A3 around the lateral slab edges. Due to the location of the low-velocity anomalies approximately below the basal lithospheric steps south and north of the Alboran Sea, edge-driven convection has been proposed as an alternative mechanism (e.g., Kaislaniemi & Van Hunen, 2014). However, because we would expect such anomalies to be of small scale and much more localized beneath the lithospheric steps, we favor our interpretation. In this framework, the two anomalies below the Betics and Rif are ultimately also fed by the material ponded below the MTZ. Seismic anisotropy measurements (Buontempo et al., 2008; Díaz et al., 2010; Miller et al., 2013) and modeling (e.g., Alpert et al., 2013) do support this hypothesis. Fast polarization directions from SKS-splitting analysis are remarkably parallel to the slow velocity anomalies beneath the Atlas Ranges, Betics, and Rif. This correlates well with the general trend of slab rollback-induced toroidal mantle flow found around the Gibraltar slab. An alternative interpretation of the low-velocity feature below A3, based on numerical modeling of the anisotropic fabric in the mantle during subduction, is that it may reflect the presence of anisotropy in the upper mantle, which can potentially bias the tomographic inversion when isotropic structure is assumed (Bezada et al., 2016). Since FMTOMO cannot account for anisotropy we are unable to rule out this hypothesis and leave it as an open hypothesis for future work.

Next, we will address whether the physical mechanisms proposed for the observed seismic low-velocity anomalies A1–A3 are thermal or chemical in nature, and whether they may contain a significant proportion of partial melt and/or water.

5.2. Nature of the Velocity Anomalies

We compare our temperature model with those of previous studies in the region from thermobarometry calculations (Thurner et al., 2014), receiver functions (Morais et al., 2015), waveform analysis (Sun et al., 2014), and geophysical-petrological modeling (Fullea et al., 2010 and personal communication).

The mantle structure below A1 shows a $T_{S,P}$ excess (after scaling) of ~100–300 °C (Figures 8d and 8j). Our inferred temperatures in the mantle are a good match with the estimates determined by geodynamic, geophysical, and petrological studies for hotspots (200 °C by Sleep, 1990; McKenzie, 1984; 215 ± 35 °C by Shilling, 1991; 200 °C by Mckenzie and O'nions, 1991; 200–300 °C by Zhao, 2001; and 162–235 °C by Putirka, 2005). These values also fall within the large thermal range suggested by *PP/SS* precursor analyses in the region, which find a temperature anomaly of ~100–300 °C for the MTZ, strongly depending on the values of the Clapeyron slope (e.g., for 4.0 MPa/K the range is 84 ± 47–327 ± 75 °C, Saki et al., 2015). Calculations from primary magma composition reveal that A1 displays some of the lowest temperatures of all the ocean-island basalt (OIB) lavas, ~1400–1500 °C (*T* excess: 100–200 °C, Herzberg & Asimow, 2008), highly consistent with our results. For OIBs, there is no evidence of volatile enrichment and source fertility. All are associated with thermal anomalies, which appear to be the only prerequisite for their

formation. According to Korenaga (2005), large mantle melting anomalies with small T excess are possible in hotspots settings such as the Canaries, due to the more fusible nature of the mantle. Several geophysical and geochemical studies (Day et al., 2010; Klügel et al., 2005; Lodge et al., 2012; Neumann et al., 2002) found shallow zones of partial melting in the western Canaries, consistent with depths of magma ponding deduced from petrological analysis and with seismic and volcanic activity (e.g., Almendros et al., 2007; Carracedo et al., 1999; De Gonzalez Vallejo et al., 2005; Soler et al., 1984). Our $a_{S,P}$ for A1 is within the expected thermal range ($a_{S,P} \approx 2.5$, $R_{S,P} \approx 1.5$), suggesting a purely thermal origin for the Canaries' upwelling. We also note that dT_S is similar to dT_P and even somewhat lower; thus, we tend to discard the hypothesis of high melt productivity at upper-mantle depths. Rather we suggest that local and shallow signatures of melt may exist, but they are not resolvable at the length scale of our inversion.

The $T_{S,P}$ excess beneath A2 is within the range ~200–350 °C, with some peaks of $dT > 400$ °C below the most prominent basaltic centers of the High and Middle Atlas (Figures 8e and 8k). Our findings are consistent with values derived from modeling of hotspots tracks beneath the continental lithosphere (~300 °C, Yang & Leng, 2014). In addition, results from seismic waveform analysis combined with geodynamic modeling reveal a strong T excess of ~350 $\pm$ 90 °C in this region (for dry mantle), which is inferred to be solely of thermal origin, although a small quantity of partial melt and volatiles may be present (Sun et al., 2014). dT_S estimates appear to be slightly higher than dT_P in the innermost parts of the low-velocity anomaly (see Figures 8e and 8k). As our tomographic models are insensitive to the effects of local melt signatures and to rapid changes in velocity over short vertical distances, we do not exclude the possibility that other physical factors, such as small melt pockets and/or water-rich layers, may be present in small quantities and/or at small spatial scales in the upper mantle. Interestingly, the $a_{S,P}$ (≈ 3.8) and $R_{S,P}$ (≈ 2.2) values found for this area are on the higher side of the thermal range and may be attributed to other nonthermal effects (e.g., different compositions, volatiles, and melt). A contribution of partial melt at shallow depths would also be consistent with magnetotelluric results (Anahnah et al., 2011) and geochemical studies (Duggen et al., 2009, 2005; El Azzouzi et al., 2010; Geldmacher et al., 2005; Hoernle et al., 1995, 1999; Lundstrom et al., 2003; Lustrino & Wilson, 2007). Receiver function analyses from Morais et al. (2015) revealed a low regional S velocity layer atop the 410-km discontinuity. One hypothesis that explains these observations is that mantle upwelling across the 410-km discontinuity leads to water release and melting atop the 410-km discontinuity (Karato et al., 2006). The melt could be buoyant and flow upward, or dense and remain stalled above the 410-km discontinuity.

The A3 region exhibits temperature anomalies from dV_P and dV_S on the order of 100–300 °C (Figures 8f and 8l). Few studies have tried to infer the temperature in the subslab domain. The petrologic results from Fullea et al. (2010) reveal a temperature of less than 1430 °C, which is consistent with the lower bound of the T excess that we find. However, from our P wave and S wave velocity models we suggest that the hot mantle rising from below A3 is dragged around the retreating Gibraltar slab through quasi-toroidal mantle flow; therefore, the mantle material below A3 and below the Rif-Betics system should be in a similar thermal range. If so, our findings are in line with thermobarometry studies (Thurner et al., 2014) that find mantle temperature estimates increasing from 1350 °C to a maximum of 1430 °C (~50–130 °C T excess), moving from the Rif to the Betics. This observation, together with the results from the residual analysis ($a_{S,P} = 2.1$, $R_{S,P} = 1.2$), thermal reconstruction, and geodynamic interpretation, leads us to propose a weak thermal signature for the mantle upwellings in the A3 region and below the Rif and Betics.

5.3. Comparison With Surface Volcanism, Heat Flow, and Lithospheric Thickness

Volcanism occurred across the Ibero-western Maghreb region from the Late Cretaceous to the present (Lustrino & Wilson, 2007). According to Missenard et al. (2006), a linear NE-SW trend of anorogenic magmatism and significant seismicity, together with thinned lithosphere and uplifted topography, the so-called Moroccan Hot Line, crosses the A2 region and cuts the eastern Rif. The magmatism continues toward southeastern Iberia and extends from the northern Moroccan passive margin into the Alboran Sea and eastern Betics. The composition of these units changes in time and space from calc-alcaline in the southern Iberia (comprising the Calatrava volcanic field) and the Alboran Sea, during the Miocene, to alkaline in the Atlas Ranges during the Pliocene and Quaternary (Duggen et al., 2004; Hoernle et al., 1995). All these volcanic centers are often viewed within the wider context of Na-rich intraplate magmatism, which characterizes the whole Euro-Mediterranean region and extends toward the eastern Atlantic

Ocean (e.g., Lustrino & Wilson, 2007; Wilson & Downes, 1991, 2006). To the west of the Strait of Gibraltar, no clear evidence of volcanic activity has been found so far above the subslab low-velocity anomaly. A recent geophysical study on the Gulf of Cadiz domain (Neres et al., 2018) imaged a magmatic intrusion offshore below the Guadalquivir Bank, which may represent the southernmost expression of the Upper Cretaceous alkaline magmatic event that affected both onshore (Sintra-Sines-Monchique igneous complexes) and offshore west Iberia. In the Atlantic domain, A1 presents a long volcanic record ranging from the oldest intraplate manifestations, occurring during the Late Cretaceous-Paleocene at just a few volcanic centers, to the recent magmatic activity in almost all the islands (e.g., Anguita & Hernán, 2000; Carracedo et al., 1999).

Surface heat flow (SHF) may play a role in generating these magmatic pockets and related temperature variations in the mantle, and lithosphere can regionally change the heat input at the base of the crust (Della Vedova et al., 2001). Rising magmas transport heat into the lithosphere by advection and can cause partial melting of lithospheric domains with lower than normal solidus temperatures in areas of active deformation. However, we should keep in mind that SHF measurements can be strongly scattered due to environmental factors, for example, water circulation and paleo-climatic variations, and can register large changes over short distances due to local geology and topography (Sclater et al., 1980).

Interestingly, the distribution of magmatic fields in the Gibraltar Arc System, Atlas Ranges, and Canaries has a first-order correlation with the low-velocity anomaly regions and T excess found in our study; conversely, no recent volcanic activity occurs where cold high-velocity anomalies are imaged. Furthermore, correlating with extensive volcanic activity, a high-averaged SHF value and a shallow lithosphere asthenosphere boundary (LAB), compared to the surrounding areas, are found. To illustrate this, we plot, in Figure 9, the magmatic centers that have been active in the last 75 Myr (from Lustrino & Wilson, 2007) together with the average of all available SHF measurements (provided by J. Fullea, personal communication) for regions A1–A3. We also include the averaged SHF values for eastern Rif and Betics, where the upward mantle flow induced by the slab rollback has been suggested to explain the vigorous Cenozoic volcanism in the Betic-Rif area. Below the top map in Figure 9, we show the LAB depth map (Fullea et al., 2010, 2015) of our S wave tomographic model and the thermal structure for regions A1–A3 derived from the S wave tomography. Below the main volcanic fields, the SHF is high on average (> 60 m/Wm^2), although some important regional variations do occur. A1 is characterized by SHF values of around 73 m/Wm^2 (see Canales & Dañobeitia, 1998), which are associated with massive volcanic outpourings (Figure 9a) and moderate lithospheric thinning (LAB depth of 90–100 km, Figure 9b). In A2, SHF values (where available) are on average of 63 m/Wm^2 (Figure 9a), in line with the strong low-velocity and positive thermal anomalies found in our study, and correlate well with the observed lithospheric thinning (80- to 120-km depth, Figure 9b). A more recent study, however, found slightly higher SHF values of about 80 m/Wm^2 below the northeastern termination of the Middle Atlas domain (Chiozzi et al., 2017). Similarly, a local measurement of 86 m/Wm^2 has been found in the southern High Atlas by Ramdani (1998), suggesting a lithosphere thickness of 50 km. When interpreted in light of these independent data, the low-velocity anomalies observed below A2 may further indicate anomalously hot upper mantle with local areas of partial melting. The highest SHF values are observed in the eastern Rif ($= \sim89$ m/Wm^2) and eastern Betics (~82 m/Wm^2, with peaks >100 m/Wm^2 in the eastern Alboran basin), where the LAB is mapped as shallow as 50–150 km (Figure 9a). This pattern of spatial coincidence between peaks in magmatic activity and strong low-velocity anomalies as imaged by our tomographic model is in good agreement with the existence of high mantle temperatures. Finally, below A3 a few SHF values have been measured in the range 50–60 m/Wm^2, which denote a moderate heat flow (Figure 9a). According to the findings in Fullea et al. (2010), the LAB in A3 is shallower than below the Alboran Sea but much deeper (~170- to 180-km depth) compared to the A2 region (Figure 9b). However, a more recent geophysical study found contradictory results, which indicate a significant lithospheric thinning below A3 (60- to 70-km depth), where low velocities are imaged (Palomeras et al., 2014). Further investigation of the A3 domain is needed to conclusively understand why the upper-mantle upwelling that we find does not show a clear volcanic expression at the surface.

Overall, the spatial distribution of surface volcanism, SHF, and depth of the LAB are in good agreement with the presence of upper-mantle thermal upwellings, which interact with the Gibraltar slab-induced mantle flow, facilitating decompression melting at sublithospheric depths and generating extensive magmatic provinces in Iberia and NW Morocco.
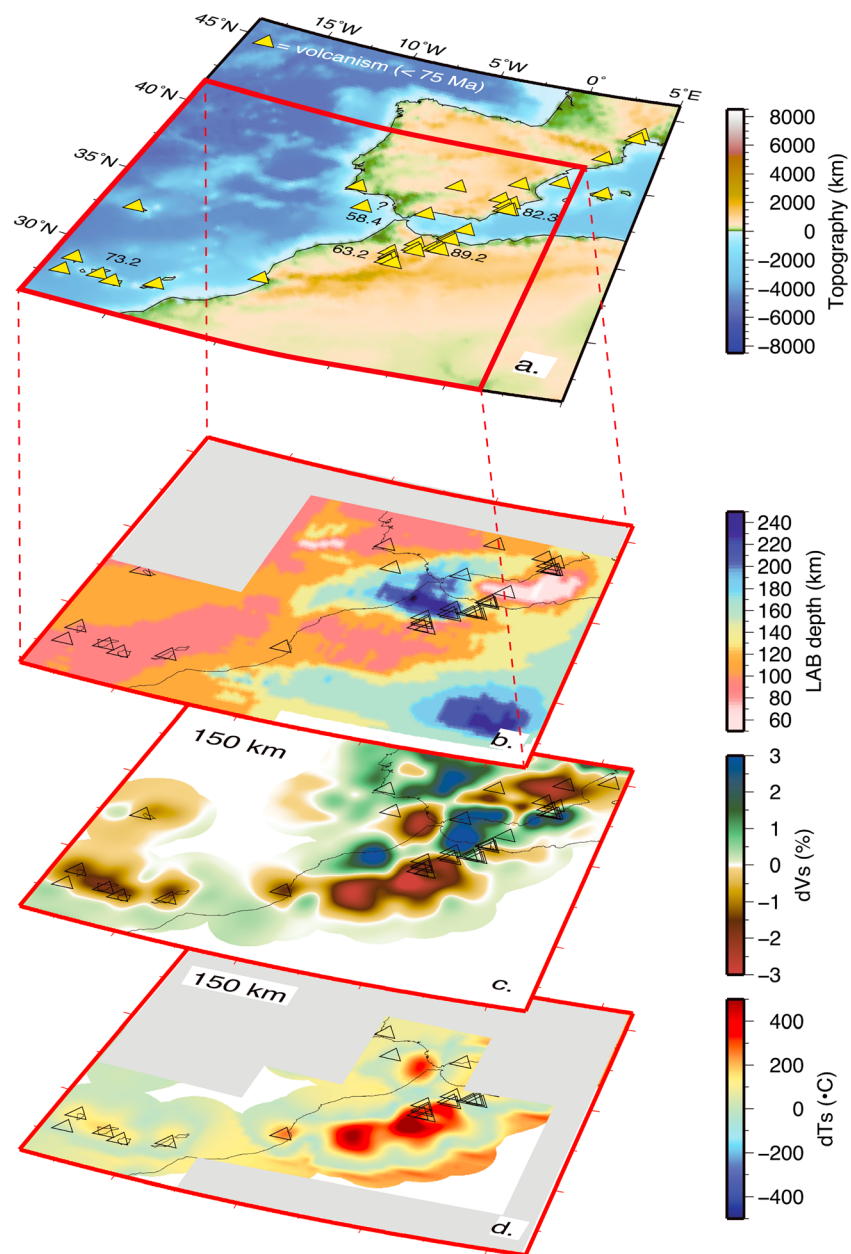
Figure 9. (a) Topography map of the Ibero-western Maghreb region with yellow triangles indicating volcanic centers from Late Cretaceous to present (modified from Lustrino & Wilson, 2007) and the averaged SHF values for A1–A3, the Rif and Betics written in black (from J. Fullea, personal communication). (b) LAB depth map (Fullea et al., 2010, 2015). (c) Our dV_S model (dV_S in percent) at 150-km depth. (d) Our scaled thermal structure for regions A1–A3 (delimitated in Figure 4a) from the S wave velocities at 150-km depth. The regions where no data are available are masked out in gray. Regions with no piercing points are shaded white. The positive temperature anomalies correlate well with the low-velocity features A1 and A2, with the thinning of the lithosphere, and at the surface with the most recent magmatic centers and highest SHF values observed. The Rif-Betics system also shows a good spatial coincidence with shallow LAB depth, SHF values, and volcanic strips. No recent volcanism and a moderate SHF are found for A3, which may result from the presence of the subducted slab. SHF = surface heat flow; LAB = lithosphere asthenosphere boundary.

6. Conclusions

We combined S wave and SKS wave data from the same networks used in our recent P wave tomography (Civiero et al., 2018) to compute a high-resolution shear-wave tomographic model of the Ibero-western Maghreb region. The S velocity features are well resolved from the surface to the base of the transition zone (extending somewhat less deep than the P wave resolution).

Our *S* wave images show subvertical low-velocity anomalies below the Canaries, the Atlas Ranges, and the Gibraltar Arc extending throughout the upper mantle. Although the resolution below the MTZ is poor, the *S* wave anomaly trends strongly resemble those of the *P* wave velocities, which suggest a lower-mantle origin. From our findings we interpret the structure as being mainly the signature of mantle upwellings rising from below the MTZ and sourced from hot material associated with the lower-mantle central Atlantic plume. Other strong low-velocity anomalies are imaged below the eastern Rif and Betics and may represent the result of the interaction between the retreating Gibraltar slab and the mantle upwelling behind it, which pushes the hot mantle material around the lateral slab edges.

The conversion of the low-velocity anomalies below the Canaries, Atlas Ranges, and Gibraltar Arc to temperature, together with analysis of arrival-time residuals, suggests that moderate temperature excesses of the order of 100–350 °C can explain the origin of these upwellings in the upper mantle. SHF observations, LAB depth estimates, and recent surface volcanism are consistent with the presence of mantle upwellings below the Canaries and Atlas Ranges. Current data availability does not allow for more definitive conclusions concerning the offshore Gibraltar Arc domain.

References

Afonso, J. C., Ranalli, G., Fernàndez, M., Griffin, W. L., O'Reilly, S. Y., & Faul, U. (2010). On the Vp/Vs-Mg# correlation in mantle peridotites: Implications for the identification of thermal and compositional anomalies in the upper mantle. *Earth and Planetary Science Letters*, *289*(3–4), 606–618. https://doi.org/10.1016/j.epsl.2009.12.005

Almendros, J., Ibáñez, J. M., Carmona, E., & Zandomeneghi, D. (2007). Array analyses of volcanic earthquakes and tremor recorded at Las Cañadas caldera (Tenerife Island, Spain) during the 2004 seismic activation of Teide volcano. *Journal of Volcanology and Geothermal Research*, *160*(3–4), 285–299. https://doi.org/10.1016/j.jvolgeores.2006.10.002

Alpert, L. A., Miller, M. S., Becker, T. W., & Allam, A. A. (2013). Structure beneath the Alboran from geodynamic flow models and seismic anisotropy. *Journal of Geophysical Research: Solid Earth*, *118*, 4265–4277. https://doi.org/10.1002/jgrb.50309

Anahnah, F., Galindo-Zaldívar, J., Chalouan, A., Pedrera, A., Ruano, P., Pous, J., et al. (2011). Deep resistivity cross section of the intraplate Atlas Mountains (NW Africa): New evidence of anomalous mantle and related Quaternary volcanism. *Tectonics*, *30*, TC5014. https://doi.org/10.1029/2010TC002859

Anguita, F., & Hernán, F. (2000). The Canary Islands origin: A unifying model. *Journal of Volcanology and Geothermal Research*, *103*(1-4), 1–26. https://doi.org/10.1016/S0377-0273(00)00195-5

Basili, R., Kastelic, V., Demircioglu, M. B., Garcia Moreno, D., Nemser, E. S., Petricca, P., et al. (2013), The European Database of Seismogenic Faults (EDSF) compiled in the framework of the Project SHARE, http://diss.rm.ingv.it/share-edsf/, 10.6092/INGV.IT-SHARE-EDSF

Bezada, M. J., Faccenda, M., & Toomey, D. R. (2016). Representing anisotropic subduction zones with isotropic velocity models: A characterization of the problem and some steps on a possible path forward. *Geochemistry, Geophysics, Geosystems*, *17*, 2825–2834. https://doi.org/10.1002/2016GC006406

Bezada, M. J., Humphreys, E. D., Davila, J. M., Carbonell, R., Harnafi, M., Palomeras, I., & Levander, A. (2014). Piecewise delamination of Moroccan lithosphere from beneath the Atlas Mountains. *Geochemistry, Geophysics, Geosystems*, *15*, 975–985. https://doi.org/10.1002/2013GC005059

Bird, P. (2003). An updated digital model of plate boundaries. *Geochemistry, Geophysics, Geosystems*, *4*(3), 1027. https://doi.org/10.1029/2001GC000252

Bolton, H., & Masters, G. (2001). Travel times of *P* and *S* from the global digital seismic networks: Implications for the relative variation of *P* and *S* velocity in the mantle. *Journal of Geophysical Research*, *106*(2000), 527–540. https://doi.org/10.1029/2000JB900378

Buontempo, L., Bokelmann, G. H. R., Barruol, G., & Morales, J. (2008). Seismic anisotropy beneath southern Iberia from SKS splitting. *Earth and Planetary Science Letters*, *273*(3–4), 237–250. https://doi.org/10.1016/j.epsl.2008.06.024

Cammarano, F., Goes, S., Deuss, A., & Giardini, D. (2005). Is a pyrolitic adiabatic mantle compatible with seismic data? *Earth and Planetary Science Letters*, *232*(3–4), 227–243. https://doi.org/10.1016/j.epsl.2005.01.031

Cammarano, F., Goes, S., Vacher, P., & Giardini, D. (2003). Inferring upper-mantle temperatures from seismic velocities. *Physics of the Earth and Planetary Interiors*, *138*(3–4), 197–222. https://doi.org/10.1016/S0031-9201(03)00156-0

Canales, J. P., & Dañobeitia, J. J. (1998). The Canary Island swell: A coherence analyses of bathymetry. *Geophysical Journal International*, *132*(March), 479–488. https://doi.org/10.1046/j.1365-246X.1998.00448.x

Carracedo, J. C., Day, S. J., Guillou, H., & Gravestock, P. (1999). Later stages of volcanic evolution of La Palma, Canary Islands, and the genesis of the Caldera de Taburiente. *Geological Society of America Bulletin*, *111*(5), 755–768. https://doi.org/10.1130/0016-7606(1999)111<0755:LSOVEO>2.3.CO;2

Carrara, G., & NEAREST Team (2008). NEAREST (2008) cruise preliminary report R/V *Urania*, 1st Aug 2008-04th Sept 2008, Technical Report ISMAR

Chiozzi, P., Barkaoui, A. E., Rimi, A., Verdoya, M., & Zarhloule, Y. (2017). A review of surface heat-flow data of the northern Middle Atlas (Morocco). *Journal of Geodynamics*, *112*, 58–71. https://doi.org/10.1016/j.jog.2017.10.003

Choukroune, P. (1989). THE ECORS Pyrenean deep seismic profile reflection data and the overall structure of an orogenic belt. *Tectonics*, *8*(1), 23–39. https://doi.org/10.1029/TC008i001p00023

Chung, D. H. (1971). Elasticity and equations of state of olivines in the Mg2SiO4-Fe2SiOS4 system. *Geophysical Journal International*, *25*(5), 511–538. https://doi.org/10.1111/j.1365-246X.1971.tb02201.x

Civiero, C., Goes, S., Hammond, J. O. S., Fishwick, S., Ahmed, A., Ayele, A., et al. (2016). Small-scale thermal upwellings under the northern East African rift from *S* travel time tomography. *Journal of Geophysical Research: Solid Earth*, *2010*, 1–14. https://doi.org/10.1002/2016JB013070

Civiero, C., Hammond, J. O. S., Goes, S., Fishwick, S., Ahmed, A., Ayele, A., et al. (2015). Multiple mantle upwellings in the transition zone beneath the northern East-African rift system from relative *P*-wave travel-time tomography. *Geochemistry, Geophysics, Geosystems*, *16*, 2949–2968. https://doi.org/10.1002/2015GC005948

Civiero, C., Strak, V., Custódio, S., Silveira, G., Rawlinson, N., Arroucau, P., & Corela, C. (2018). A common deep source for upper-mantle upwellings below the Ibero-western Maghreb region from teleseismic *P*-wave travel-time tomography. *Earth and Planetary Science Letters*, *499*, 157–172. https://doi.org/10.1016/j.epsl.2018.07.024

Currie, C. A., & Hyndman, R. D. (2006). The thermal structure of subduction zone back arcs. *Journal of Geophysical Research*, *111*, B08404. https://doi.org/10.1029/2005JB004024

Custódio, S., Dias, N. A., Caldeira, B., Carrilho, F., Carvalho, S., Corela, C., et al. (2014). Ambient noise recorded by a dense broadband seismic deployment in western Iberia. *Bulletin of the Seismological Society of America*, *104*(6), 2985–3007. https://doi.org/10.1785/0120140079

Day, J. M. D., Pearson, D. G., Macpherson, C. G., Lowry, D., & Carracedo, J. C. (2010). Evidence for distinct proportions of subducted oceanic crust and lithosphere in HIMU-type mantle beneath El Hierro and La Palma, Canary Islands. *Geochimica et Cosmochimica Acta*, *74*(22), 6565–6589. https://doi.org/10.1016/j.gca.2010.08.021

De Gonzalez Vallejo, L. I., Capote, R., Cabrera, L., Insua, J. M., & Acosta, J. (2005). Paleoearthquake evidence in Tenerife (Canary Islands) and possible seismotectonic sources. *Geophysics of the Canary Islands: Results of Spain's Exclusive Economic Zone Program*, *2003*, 149–160. https://doi.org/10.1007/1-4020-4352-X_7

Della Vedova, B., Bellani, S., Pellis, G., & Squarci, P. (2001). Deep temperatures and surface heat flow distribution. In G. B. Vai & P. Martini (Eds.), *The Apennines: Anatomy of an orogen*, (pp. 65–76 + 2 Maps). Kluwer Academic Publishers: Dordrecht.

Deschamps, F., & Trampert, J. (2003). Mantle tomography and its relation to temperature and composition. *Physics of the Earth and Planetary Interiors*, *140*(4), 277–291. https://doi.org/10.1016/j.pepi.2003.09.004

Dias, N.A., Silveira, G., & Haberland, C. (2010). Data of the temporary seismic WILAS network. GFZ Data Services. Other/Seismic Network. https://doi.org/10.14470/3N7565750319

Díaz, J., Gallart, J., & TopoIberia Seismic Working Group Team (2009). SKS splitting in southern Iberia and northern Morocco: First contributions of the IBERARRAY broadband seismic network. *Geophysical Research Abstracts*, *11*, EGU2009-7376-1.

Díaz, J., Gallart, J., Villaseñor, A., Mancilla, F., Pazos, A., Córdoba, D., et al. (2010). Mantle dynamics beneath the Gibraltar arc (western Mediterranean) from shear-wave splitting measurements on a dense seismic array. *Geophysical Research Letters*, *37*, L18304. https://doi.org/10.1029/2010GL044201

Duggen, S., Hoernle, K., van den Bogaard, P., & Garbe-Schönberg, D. (2005). Post-collisional transition from subduction-to intraplate-type magmatism in the westernmost Mediterranean: Evidence for continental-edge delamination of subcontinental lithosphere. *Journal of Petrology*, *46*(6), 1155–1201. https://doi.org/10.1093/petrology/egi013

Duggen, S., Hoernle, K., van den Bogaard, P., & Harris, C. (2004). Magmatic evolution of the Alboran region: The role of subduction in forming the western Mediterranean and causing the Messinian salinity crisis. *Earth and Planetary Science Letters*, *218*(1–2), 91–108. https://doi.org/10.1016/S0012-821X(03)00632-0

Duggen, S., Hoernle, K. A., Hauff, F., Klügel, A., Bouabdellah, M., & Thirlwall, M. F. (2009). Flow of Canary mantle plume material through a subcontinental lithospheric corridor beneath Africa to the Mediterranean. *Geology*, *37*(3), 283–286. https://doi.org/10.1130/G25426A.1

El Azzouzi, E., El, M., Mohammed, A., Universit, M., Occidentale, B., Universit, B., & Occidentale, B. (2010). Petrology and K-Ar chronology of the Neogene-Quaternary middle Atlas basaltic province, Morocco. *Bulletin de La Société Géologique de France*, *181*(3), 243–257. https://doi.org/10.2113/gssgfbull.181.3.243

Faul, U. H., & Jackson, I. (2002). Grain-size-sensitive seismic wave attenuation in polycrystalline olivine. *Journal of Geophysical Research*, *107*(B12), 2360. https://doi.org/10.1029/2001JB001225

Fontboté, J. M., Guimera, J., Roca, E., Sabat, F., & Santanach, P. (1990). The Cenozoic geodynamic evolution of the Valencia trough (western Mediterranean). *Revista de la Sociedad Geológica de España*, *3*, 249–259.

Forte, A. M., & Perry, H. K. C. (2000). Geodynamic evidence for a chemically depleted continental tectosphere. *Science*, *290*(5498), 1940–1944. https://doi.org/10.1126/science.290.5498.1940

French, S. W., Lekić, V., & Romanowicz, B. (2013). Waveform tomography reveals channeled flow at the base of the oceanic asthenosphere. *Science*, *355*(6359), 437–440. https://doi.org/10.1038/355437a0

Fullea, J., Camacho, A. G., Negredo, A. M., & Fernández, J. (2015). The Canary Islands hot spot: New insights from 3D coupled geophysical-petrological modelling of the lithosphere and uppermost mantle. *Earth and Planetary Science Letters*, *409*, 71–88. https://doi.org/10.1016/j.epsl.2014.10.038

Fullea, J., Fernàndez, M., Afonso, J. C., Vergés, J., & Zeyen, H. (2010). The structure and evolution of the lithosphere-asthenosphere boundary beneath the Atlantic-Mediterranean transition region. *Lithos*, *120*(1–2), 74–95. https://doi.org/10.1016/j.lithos.2010.03.003

Funiciello, F., Moroni, M., Piromallo, C., Faccenna, C., Cenedese, A., & Bui, H. A. (2006). Mapping mantle flow during retreating subduction: Laboratory models analyzed by feature tracking. *Journal of Geophysical Research*, *111*, B03402. https://doi.org/10.1029/2005JB003792

Gao, W., Grand, S. P., Baldridge, W. S., Wilson, D., West, M., Ni, J., & Aster, R. (2004). Upper mantle convection beneath the central Rio Grande rift imaged by *P* and *S* wave tomography. *Journal of Geophysical Research*, *109*, B03305. https://doi.org/10.1029/2003JB002743

García-Mayordomo, J., Insua-Arévalo, J. M., Martínez-Díaz, J. J., Jiménez-Díaz, A., Martín-Banda, R., Martín-Alfageme, S., Álvarez-Gómez, J. A., et al. (2012). The Quaternary active faults database of Iberia (QAFI v. 2.0). *Journal of Iberian Geology*, *38*(1), 285–302. https://doi.org/10.5209/rev_JIGE.2012.v38.n1.39219

Geldmacher, J., Hoernle, K., Bogaard, P. V. D., Duggen, S., & Werner, R. (2005). New [40]Ar/[39]Ar age and geochemical data from seamounts in the Canary and Madeira volcanic provinces: Support for the mantle plume hypothesis. *Earth and Planetary Science Letters*, *237*(1–2), 85–101. https://doi.org/10.1016/j.epsl.2005.04.037

GEOFON Data Centre (1993). GEOFON seismic network. Deutsches GeoForschungsZentrum GFZ. Other/Seismic Network. https://doi.org/10.14470/TR560404

Gibbons, W., & Moreno, T. (2002). *The geology of Spain*. London: Geol. Soc.

Goes, S., Cammarano, F., & Hansen, U. (2004). Synthetic seismic signature of thermal mantle plumes. *Earth and Planetary Science Letters*, *218*(3–4), 403–419. https://doi.org/10.1016/S0012-821X(03)00680-0

Goes, S., Govers, R., & Vacher, P. (2000). Shallow mantle temperatures under Europe from *P* and *S* wave tomography. *Journal of Geophysical Research*, *105*(B5), 11153–11169. https://doi.org/10.1029/1999JB900300

Goes, S., Simons, F. J., & Yoshizawa, K. (2005). Seismic constraints on temperature of the Australian uppermost mantle. *Earth and Planetary Science Letters*, *236*(1–2), 227–237. https://doi.org/10.1016/j.epsl.2005.05.001

Goes, S., & van der Lee, S. (2002). Thermal structure of the North American uppermost mantle inferred from seismic tomography. *Journal of Geophysical Research*, *107*(B3), 2050. https://doi.org/10.1029/2000JB000049

Gutscher, M. A., Malod, J., Rehault, J. P., Contrucci, I., Klingelhoefer, F., Mendes-Victor, L., & Spakman, W. (2002). Evidence for active subduction beneath Gibraltar. *Geology*, *30*(12), 1071–1074. https://doi.org/10.1130/0091-7613(2002)030<1071:EFASBG>2.0.CO;2

Hales, A. L., & Doyle, H. A. (1967). *P* and *S* travel time anomalies and their interpretation. *Geophysical Journal of the Royal Astronomical Society*, *13*(4), 403–415. https://doi.org/10.1111/j.1365-246X.1967.tb03139.x

Hammond, W. C., & Humphreys, E. D. (2000). Upper mantle seismic wave attenuation: Effects of realistic partial melt distribution. *Journal of Geophysical Research*, *105*(B5), 10987–10999. https://doi.org/10.1029/2000JB900042

Herzberg, C., & Asimow, P. D. (2008). Petrology of some oceanic island basalts: PRIMELT2.XLS software for primary magma calculation. *Geochemistry, Geophysics, Geosystems*, *9*, Q09001. https://doi.org/10.1029/2008GC002057

Hoernle, K., van den Bogaard, P., Duggen, S., Mocek, B., & Garbe-Schönberg, D. (1999). Evidence for Miocene subduction beneath the Alboran Sea: 40Ar/39Ar dating and geochemistry of volcanic rocks from Holes 977A and 978A. *Proceedings of the Ocean Drilling Program*, *161*, 357–373. https://doi.org/10.2973/odp.proc.sr.161.264.1999

Hoernle, K., Zhang, Y.-S., & Graham, D. (1995). Seismic and geochemical evidence for large-scale mantle upwelling beneath the eastern Atlantic and western and central Europe. *Nature*, *374*(6517), 34–39. https://doi.org/10.1038/374034a0

Institut Cartogràfic i Geològic de Catalunya-Institut d'Estudis Catalans (1996). Catalan seismic network. International Federation of Digital Seismograph Networks. 10.7914/SN/CA

Institute Earth Sciences "Jaume Almera" CSIC (ICTJA Spain) (2007). IberArray. International Federation of Digital Seismograph Networks. Other/Seismic Network 10.7914/SN/IB

Kaislaniemi, L., & Van Hunen, J. (2014). Dynamics of lithospheric thinning and mantle melting by edge-driven convection: Application to Moroccan Atlas Mountains. *Geochemistry, Geophysics, Geosystems*, *158*, 3175–3189. https://doi.org/10.1002/2015GC005918

Karato, S., & Jung, H. (1998). Water, partial melting and the origin of the seismic low velocity and high attenuation zone in the upper mantle. *Earth and Planetary Science Letters*, *157*(3–4), 193–207. https://doi.org/10.1016/S0012-821X(98)00034-X

Karato, S., & Karki, B. B. (2001). Origin of lateral variation of seismic wave velocities and density in the deep mantle. *Journal of Geophysical Research*, *106*, 771–783. https://doi.org/10.1029/2001JB000214

Karato, S.-I., Bercovici, D., Leahy, G., Richard, G., & Jing, Z. (2006). The transition-zone water filter model for global material circulation: Where do we stand? *Geophysical Monograph Series*, *168*, 289–313. https://doi.org/10.1029/168GM22

Kennett, B. L. N., & Engdahl, E. R. (1991). Traveltimes for global earthquake location and phase identification. *Geophysical Journal International*, *105*(2), 429–465. https://doi.org/10.1111/j.1365-246X.1991.tb06724.x

Kennett, B. L. N., Engdahl, E. R., & Buland, R. (1995). Constraints on seismic velocities in the Earth from travel times. *Geophysical Journal International*, *122*(1), 108–124. https://doi.org/10.1111/j.1365-246X.1995.tb03540.x

Kennett, B. L. N., Sambridge, M., & Williamson, P. R. (1988). Subspace methods for large inverse problems with multiple parameter classes. *Geophysical Journal International*, *94*(2), 237–247. https://doi.org/10.1111/j.1365-246X.1988.tb05898.x

Klügel, A., Hansteen, T. H., & Galipp, K. (2005). Magma storage and underplating beneath Cumbre Vieja volcano, La Palma (Canary Islands). *Earth and Planetary Science Letters*, *236*(1–2), 211–226. https://doi.org/10.1016/j.epsl.2005.04.006

Koper, K. D., Wiens, D. A., Dorman, L., Hildebrand, J., & Webb, S. (1999). Constraints on the origin of slab and mantle wedge anomalies in Tonga from the ratio of *S* to *P* velocities. *Journal of Geophysical Research*, *104*(B7), 15089–15104. https://doi.org/10.1029/1999JB900130

Korenaga, J. (2005). Firm mantle plumes and the nature of the core-mantle boundary region. *Earth and Planetary Science Letters*, *232*(1–2), 29–37. https://doi.org/10.1016/j.epsl.2005.01.016

Kumagai, I., Davaille, A., & Kurita, K. (2007). On the fate of thermally buoyant mantle plumes at density interfaces. *Earth and Planetary Science Letters*, *254*(1–2), 180–193. https://doi.org/10.1016/j.epsl.2006.11.029

Levander, A., Bezada, M. J., Niu, F., Humphreys, E. D., Palomeras, I., Thurner, S. M., et al. (2014). Subduction-driven recycling of continental margin lithosphere. *Nature*, *515*(7526), 253–256. https://doi.org/10.1038/nature13878

Levander, A., Humphreys, G., & Ryan, P. (2009). Program to investigate convective Alboran Sea system overturn. International Federation of Digital Seismograph Networks. Other/Seismic Network. 10.7914/SN/XB_2009

Lodge, A., Nippress, S. E. J., Rietbrock, A., García-Yeguas, A., & Ibáñez, J. M. (2012). Evidence for magmatic underplating and partial melt beneath the Canary Islands derived using teleseismic receiver functions. *Physics of the Earth and Planetary Interiors*, *212–213*, 44–54. https://doi.org/10.1016/j.pepi.2012.09.004

Lonergan, L., & White, N. (1997). Origin of the Betic-Rif mountain belt. *Tectonics*, *16*(3), 504–522. https://doi.org/10.1029/96TC03937

Lundstrom, C. C., Hoernle, K., & Gill, J. (2003). U-series disequilibria in volcanic rocks from the Canary Islands: Plume versus lithospheric melting. *Geochimica et Cosmochimica Acta*, *67*(21), 4153–4177. https://doi.org/10.1016/S0016-7037(03)00308-9

Lustrino, M., & Wilson, M. (2007). The circum-Mediterranean anorogenic Cenozoic igneous province. *Earth-Science Reviews*, *81*(1-2), 1–65. https://doi.org/doi:10.1016/j.earscirev.2006.09.002

Masters, G., Laske, G., Bolton, H., & Dziewonski, A. (2000). The relative behavior of shear velocity, bulk sound speed, and Earth's deep interior. In Karato et al. (Eds.), *Mineral Physics and Tomography from the Atomic to the Global Scale*, *Geophysical Monograph Series* (Vol. 117, pp. 63–87). Washington, DC: American Geophysical Union. https://doi.org/10.1029/GM117p0063

McKenzie, D. (1984). The generation and compaction of partially molten rock. *Journal of Petrology*, *25*(3), 713–765. https://doi.org/10.1093/petrology/25.3.713

Mckenzie, D., & O'nions, R. K. (1991). Partial melt distributions from inversion of rare earth element concentrations. *Journal of Petrology*, *32*(5), 1021–1091. https://doi.org/10.1093/petrology/32.5.1021

MedNet Project Partner Institutions (1990). January 1. In *Mediterranean very broadband seismographic network (MedNet)*. Italy: Istituto Nazionale di Geofisica e Vulcanologia (INGV). https://doi.org/10.13127/sd/fbbbtdtd6q

Miller, M. S., Allam, A. A., Becker, T. W., Di Leo, J. F., & Wookey, J. (2013). Constraints on the tectonic evolution of the westernmost Mediterranean and northwestern Africa from shear wave splitting analysis. *Earth and Planetary Science Letters*, *375*, 234–243. https://doi.org/10.1016/j.epsl.2013.05.036

Miller, M. S., Driscoll, L. J. O., Butcher, A. J., & Thomas, C. (2015). Imaging Canary Island hotspot material beneath the lithosphere of Morocco and southern Spain. *Earth and Planetary Science Letters*, *431*, 186–194. https://doi.org/10.1016/j.epsl.2015.09.026

Missenard, Y., & Cadoux, A. (2012). Can Moroccan Atlas lithospheric thinning and volcanism be induced by edge-driven convection? *Terra Nova*, *24*(1), 27–33. https://doi.org/10.1111/j.1365-3121.2011.01033.x

Missenard, Y., Zeyen, H., de Lamotte, D. F., Leturmy, P., Petit, C., Sébrier, M., & Saddiqi, O. (2006). Crustal versus asthenospheric origin of relief of the Atlas Mountains of Morocco. *Journal of Geophysical Research*, *111*, B03401. https://doi.org/10.1029/2005JB003708

Morais, I., Vinnik, L., Silveira, G., Kiselev, S., & Matias, L. (2015). Mantle beneath the Gibraltar arc from receiver functions. *Geophysical Journal International*, *200*, 1155–1171. https://doi.org/10.1093/gji/ggu456

Neres, M., Terrinha, P., Custódio, S., Silva, S. M., Luis, J., & Miranda, J. M. (2018). Geophysical evidence for a magmatic intrusion in the ocean-continent transition of the SW Iberia margin. *Tectonophysics*, *744*, 118–133. https://doi.org/10.1016/j.tecto.2018.06.014

Neumann, E. R., Wulff-Pedersen, E., Pearson, N. J., & Spencer, E. a. (2002). Mantle xenoliths from Tenerife (Canary Islands): Evidence for reactions between mantle peridotites and silicic carbonatite melts inducing Ca metasomatism. *Journal of Petrology*, *43*(5), 825–857. https://doi.org/10.1093/petrology/43.5.825

Palomeras, I., Thurner, S., Levander, A., & Liu, K. (2014). Finite-frequency Rayleigh wave tomography of the western Mediterranean: Mapping its lithospheric structure. *Geochemistry, Geophysics, Geosystems*, *15*, 140–160. https://doi.org/10.1002/2013GC004861

Papaleo, E., Cornwell, D., & Rawlinson, N. (2018). Constraints on North Anatolian fault zone width in the crust and upper mantle from *S* wave teleseismic tomography. *Journal of Geophysical Research: Solid Earth*, *123*, 2908–2922. https://doi.org/10.1002/2017JB015386

Peter, D., Boschi, L., Deschamps, F., Fry, B., Ekström, G., & Giardini, D. (2008). A new finite-frequency shear-velocity model of the European-Mediterranean region. *Geophysical Research Letters*, *35*, L16315. https://doi.org/10.1029/2008GL034769

Piromallo, C., Becker, T. W., Funiciello, F., & Faccenna, C. (2006). Three-dimensional instantaneous mantle flow induced by subduction. *Geophysical Research Letters*, *33*, L08304. https://doi.org/10.1029/2005GL025390

Platt, J. P., Becker, T. W., Evans, T. R. L., Humphreys, E. D., Lee, C.-T., & Levander, A. (2008). PICASSO: Testing models for upper mantle processes beneath the Alboran basin and the Gibraltar arc (western Mediterranean). In *AGU General Assembly* (Vol. 40, p. 273). San Francisco, CA: American Geosciences Union.

Putirka, K. D. (2005). Mantle potential temperatures at Hawaii, Iceland, and the mid-ocean ridge system, as inferred from olivine phenocrysts: Evidence for thermally driven mantle plumes. *Geochemistry, Geophysics, Geosystems*, *6*, Q05L08. https://doi.org/10.1029/2005GC000915

Ramdani, F. (1998). Geodynamic implications of intermediate-depth earthquakes and volcanism in the intraplate Atlas Mountains (Morocco). *Physics of the Earth and Planetary Interiors*, *108*(3), 245–260. https://doi.org/10.1016/S0031-9201(98)00106-X

Rawlinson, N., & Kennett, B. L. N. (2004). Rapid estimation of relative and absolute delay times across a network by adaptive stacking. *Geophysical Journal International*, *157*(1), 332–340. https://doi.org/10.1111/j.1365-246X.2004.02188.x

Rawlinson, N., Pozgay, S., & Fishwick, S. (2010). Seismic tomography: A window into deep Earth. *Physics of the Earth and Planetary Interiors*, *178*(3–4), 101–135. https://doi.org/10.1016/j.pepi.2009.10.002

Rawlinson, N., Reading, A. M., & Kennett, B. L. N. (2006). Lithospheric structure of Tasmania from a novel form of teleseismic tomography. *Journal of Geophysical Research*, *111*, B02301. https://doi.org/10.1029/2005JB003803

Rawlinson, N., & Sambridge, M. (2004a). Multiple reflection and transmission phases in complex layered media using a multistage fast marching method. *Geophysics*, *69*(5), 1338–1350. https://doi.org/10.1190/1.1801950

Rawlinson, N., & Sambridge, M. (2004b). Wave front evolution in strongly heterogeneous layered media using the fast marching method. *Geophysical Journal International*, *156*(3), 631–647. https://doi.org/10.1111/j.1365-246X.2004.02153.x

Resovsky, J., & Trampert, J. (2003). Using probabilistic seismic tomography to test mantle velocity-density relationships. *Earth and Planetary Science Letters*, *215*(1–2), 121–134. https://doi.org/10.1016/S0012-821X(03)00436-9

Robertson, G. S., & Woodhouse, J. H. (1996). Ratio of relative *S* to *P* velocity heterogeneity in the lower mantle. *Journal of Geophysical Research*, *101*(20), 20,041–20,052. https://doi.org/10.1029/96JB01905

Rocha, M. P., Schimmel, M., & Assumpção, M. (2011). Upper-mantle seismic structure beneath SE and Central Brazil from *P*- and *S*-wave regional traveltime tomography. *Geophysical Journal International*, *184*(1), 268–286. https://doi.org/10.1111/j.1365-246X.2010.04831.x

Saki, M., Thomas, C., Nippress, S. E. J., & Lessing, S. (2015). Topography of upper mantle seismic discontinuities beneath the North Atlantic: The Azores, Canary and Cape Verde plumes. *Earth and Planetary Science Letters*, *409*, 193–202. https://doi.org/10.1016/j.epsl.2014.10.052

Saltzer, R. L., Van der Hilst, R. D., & Kárason, H. (2001). Comparing *P* and *S* wave heterogeneity in the mantle. *Geophysical Research Letters*, *28*(7), 1335–1338. https://doi.org/10.1029/2000GL012339

San Fernando Royal Naval Observatory (ROA), Universidad Complutense De Madrid (UCM), Helmholtz-Zentrum Potsdam Deutsches GeoForschungsZentrum (GFZ), Universidade De Evora (UEVORA, Portugal), & Institute Scientifique Of RABAT (ISRABAT, Morocco) (1995). The western Mediterranean BB seismic network. Deutsches GeoForschungsZentrum GFZ. Other/Seismic Network. https://doi.org/10.14470/JZ581150

Schivardi, R., & Morelli, A. (2009). Surface wave tomography in the European and Mediterranean region. *Geophysical Journal International*, *177*(3), 1050–1066. https://doi.org/10.1111/j.1365-246X.2009.04100.x

Schmandt, B., & Humphreys, E. (2010a). Complex subduction and small-scale convection revealed by body-wave tomography of the western United States upper mantle. *Earth and Planetary Science Letters*, *297*(3–4), 435–445. https://doi.org/10.1016/j.epsl.2010.06.047

Schmandt, B., & Humphreys, E. (2010b). Seismic heterogeneity and small-scale convection in the southern California upper mantle. *Geochemistry, Geophysics, Geosystems*, *11*, Q05004. https://doi.org/10.1029/2010GC003042

Sclater, J. G., Jaupart, C., & Galson, D. (1980). The heat flow through oceanic and continental crust and the heat loss of the Earth. *Reviews of Geophysics and Space Physics*, *18*(1), 269–311. https://doi.org/10.1029/RG018i001p00269

Shilling, J. (1991). Fluxes and excess temperatures of mantle plumes inferred from their interaction with migrating mid-ocean ridges. *Nature*, *352*(6334), 397–403. https://doi.org/10.1038/352397a0

Simmons, N. A., Forte, A. M., & Grand, S. P. (2009). Joint seismic, geodynamic and mineral physical constraints on three-dimensional mantle heterogeneity: Implications for the relative importance of thermal versus compositional heterogeneity. *Geophysical Journal International*, *177*(3), 1284–1304. https://doi.org/10.1111/j.1365-246X.2009.04133.x

Simmons, N. A., Myers, S. C., Johannesson, G., & Matzel, E. (2012). LLNL-G3Dv3: Global P wave tomography model for improved regional and teleseismic travel time prediction. *Journal of Geophysical Research*, *117*, B10302. https://doi.org/10.1029/2012JB009525

Sleep, N. H. (1990). Hotspots and mantle plumes: Some phenomenology. *Geology*, *95*, 6715–6736. https://doi.org/10.1029/JB095iB05p06715

Smith, W. H., & Sandwell, D. (1997). Global sea floor topography from satellite altimetry and ship depth soundings. *Science*, *277*(5334), 1956–1962. https://doi.org/10.1126/science.277.5334.1956

Sobolev, S. V., Zeyen, H., Granet, M., Achauer, U., Bauer, C., Werling, F., et al. (1997). Upper mantle temperatures and lithosphere-asthenosphere system beneath the French massif central constrained by seismic, gravity, petrologic and thermal observations. *Tectonophysics*, *275*(1-3), 143–164. https://doi.org/10.1016/S0040-1951(97)00019-X

Sobolev, S. V., Zeyen, H., Stoll, G., Werling, F., Altherr, R., & Fuchs, K. (1996). Upper mantle temperatures from teleseismic tomography of French massif central including effects of composition, mineral reactions, anharmonicity, anelasticity and partial melt. *Earth and Planetary Science Letters*, *139*(1-2), 147–163. https://doi.org/10.1016/0012-821X(95)00238-8

Soler, V., Carracedo, J. C., & Heller, F. (1984). Geomagnetic secular variation in historical lavas from the Canary Islands. *Geophysical Journal of the Royal Astronomical Society*, *78*(1), 313–318. https://doi.org/10.1111/j.1365-246X.1984.tb06487.x

Strak, V., & Schellart, W. P. (2014). Evolution of 3-D subduction-induced mantle flow around lateral slab edges in analogue models of free subduction analysed by stereoscopic particle image velocimetry technique. *Earth and Planetary Science Letters*, *403*, 368–379. https://doi.org/10.1016/j.epsl.2014.07.007

Styles, E., Goes, S., van Keken, P. E., Ritsema, J., & Smith, H. (2011). Synthetic images of dynamically predicted plumes and comparison with a global tomographic model. *Earth and Planetary Science Letters*, *311*(3–4), 351–363. https://doi.org/10.1016/j.epsl.2011.09.012

Sun, D., Miller, M. S., Holt, A. F., & Becker, T. W. (2014). Hot upwelling conduit beneath the Atlas Mountains, Morocco. *Geophysical Research Letters*, *391*, 212–223. https://doi.org/10.1002/2014GL061884

Takei, Y. (2002). Effect of pore geometry on V P/V S: From equilibrium geometry to crack. *Journal of Geophysical Research*, *107*(B2), 2043. https://doi.org/10.1029/2001JB000522

Thomas, C. (2010). Morocco-Muenster. International Federation of Digital Seismograph Networks. Other/Seismic Network. 10.7914/SN/3D_2010

Thurner, S., Palomeras, I., Levander, A., Carbonell, R., & Lee, C. T. (2014). Ongoing lithospheric removal in the western Mediterranean: Evidence from Ps receiver functions and thermobarometry of Neogene basalts (PICASSO project). *Geochemistry, Geophysics, Geosystems*, *15*, 1113–1127. https://doi.org/10.1002/2013GC005124

Tosi, N., & Yuen, D. A. (2011). Bent-shaped plumes and horizontal channel flow beneath the 660 km discontinuity. *Earth and Planetary Science Letters*, *312*(3–4), 348–359. https://doi.org/10.1016/j.epsl.2011.10.015

Van Wijk, J., Van Hunen, J., & Goes, S. (2008). Small-scale convection during continental rifting: Evidence from the Rio Grande rift. *Geology*, *36*(7), 575–578. https://doi.org/10.1130/G24691A.1

Vilanova, S. P., Nemser, E. S., Besana-Ostman, G. M., Bezzeghoud, M., Borges, J. F., da Silveira, A. B., et al. (2014). Incorporating descriptive metadata into seismic source zone models for seismic-hazard assessment: A case study of the Azores–West Iberian region. *Bulletin of the Seismological Society of America*, *104*(3), 1212–1229. https://doi.org/10.1785/0120130210

Wilson, M., & Downes, H. (1991). Tertiary - Quarternary extension-related alkaline magmatism in western and central Europe. *Journal of Petrology*, *32*(4), 811–849. https://doi.org/10.1093/petrology/32.4.811

Wilson, M., & Downes, H. (2006). Tertiary-Quaternary intra-plate magmatism and mantle dynamics in Europe. *Geological Society, London, Memoirs*, *32*(1), 147–166. https://doi.org/10.1144/GSL.MEM.2006.032.01.09

Xu, W., Lithgow-Bertelloni, C., Stixrude, L., & Ritsema, J. (2008). The effect of bulk composition and temperature on mantle seismic structure. *Earth and Planetary Science Letters*, *275*(1–2), 70–79. https://doi.org/10.1016/j.epsl.2008.08.012

Yan, B., Graham, E. K., & Furlong, K. P. (1989). Lateral variations in upper mantle thermal structure inferred from three-dimensional seismic inversion models. *Geophysical Research Letters*, *16*(5), 449–452. https://doi.org/10.1029/GL016i005p00449

Yang, T., & Leng, W. (2014). Dynamics of hidden hotspot tracks beneath the continental lithosphere. *Earth and Planetary Science Letters*, *401*, 294–300. https://doi.org/10.1016/j.epsl.2014.06.019

Zeyen, H., Ayarza, P., Fernàndez, M., & Rimi, A. (2005). Lithospheric structure under the western African-European plate boundary: A transect across the Atlas Mountains and the Gulf of Cadiz. *Tectonics*, *24*, TC2001. https://doi.org/10.1029/2004TC001639

Zhao, D. (2001). Seismic structure and origin of hotspots and mantle plumes. *Earth and Planetary Science Letters*, *192*(3), 251–265. https://doi.org/10.1016/S0012-821X(01)00465-4

Zitellini, N., Gràcia, E., Matias, L., Terrinha, P., Abreu, M. A., De Alteriis, G., et al. (2009). The quest for the Africa-Eurasia plate boundary west of the Strait of Gibraltar. *Earth and Planetary Science Letters*, *280*(1–4), 13–50. https://doi.org/10.1016/j.epsl.2008.12.005